Momentum Transfer between Semidiurnal Internal Waves and Subinertial Flow at a Dissipating Surface Reflection

by

Reyna L. Jenkyns
Bachelor of Mathematics, University of Waterloo, 2006

A Thesis Submitted in Partial Fulfillment of the
Requirements for the Degree of

MASTER OF SCIENCE

in the Department of Earth and Ocean Sciences

Momentum Transfer between Semidiurnal Internal Waves and Subinertial Flow at a Dissipating Surface Reflection

by

Reyna L. Jenkyns
BMath, University of Waterloo, 2006

Supervisory Committee

Dr. Eric L. Kunze (Department of Earth and Ocean Sciences)

Supervisor

Dr. Chris Garrett (Department of Earth and Ocean Sciences)

Committee Member

Supervisory Committee

Dr. Eric L. Kunze (Department of Earth and Ocean Sciences)

Supervisor

Dr. Chris Garrett (Department of Earth and Ocean Sciences)

Committee Member

Abstract

Full-depth profile data reveal semidiurnal internal waves radiating from Mendocino Escarpment. Energy- and momentum-fluxes are lost between stations bracketing the first surface reflection to the north. A plausible interpretation is that wave energy is dissipated as a consequence of superposition of incident and reflected waves. Because there are no profiler data in the superposition region, a theoretical approach is used to bridge the gap. Assuming zonal independence, constant stratification and linear decay in the dissipation region, the forcing on the mean equations is evaluated with parameters consistent with Mendocino Escarpment data. Both superposition and dissipation cause momentum-flux divergence forcing. An Ekman-like balance is anticipated with predicted mean zonal flows $\overline{u}$ $\sim$O(1-2 cm/s), comparable to surface wind-forced Ekman currents.

Contents

List of Tables

List of Figures

Acknowledgements

This work would not have been possible without the guidance of my thesis supervisor, Dr. Eric Kunze, who helped me to understand internal waves and their complexities. I am especially grateful for the field research opportunities which gave me an appreciation for the challenges in collecting data at sea. Dr. Chris Garrett and Dr. Jody Klymak also provided helpful criticisms and strategies, particularly with regard to the theoretical development, at numerous stages along the way. I cannot neglect thanking my employers from the past year, AXYS Technologies and NEPTUNE Canada, for being flexible with my graduate study commitments. Special thanks to my family and my boyfriend, Robin Deeley, for their constant support and patience.

Reyna L. Jenkyns

Chapter 1

Introduction

The role of momentum transfer between internal waves and subinertial flow in the ocean is not well understood. Internal wave momentum-fluxes, sometimes described as Reynolds stresses, are the rate of momentum transfer across a unit area by the perturbation velocity (LeBlond and Mysak, 1978). Their divergences appear as forcing terms in the time-mean equations of motion (after using a Reynolds decomposition and averaging over a wave period) and are often assumed negligible. This assumption follows from the fact that consistency relations for freely propagating non-dissipative internal waves yield cancellations between the momentum-flux divergences. This simplification is not always valid, particularly in regions where waves dissipate (Garrett, 1968; Bretherton, 1969; Muench and Kunze, 1999 and 2000; Holton and Alexander, 2000) or interact with each other. However, there is no generalized theory to describe forcing of subinertial flow due to internal waves.

Surveying the literature on wave-mean momentum transfer is complicated by the varied nomenclature: wave drag, form drag, Reynolds-stress,

remote recoil, pseudo-momentum, momentum-flux divergence and deposition of momentum-flux. Our study, motivated by measurements at Mendocino Escarpment, shows dissipation and wave-wave interactions both influence mean flow associated with an internal tide beam reflecting off the surface in a rotating frame. Internal tides are a natural choice to examine since they are associated with a peak in the internal wave energy spectrum and substantial localized mixing events.

Near the first surface reflection of a semidiurnal internal wave beam generated at Mendocino Escarpment, Althaus et al. (2003) reported a decrease in the northward horizontal depth-integrated energy-flux from 4 to 2 kW/m and inferred elevated near-surface turbulent dissipation rates ε greater than 10^{-8} W/kg. A plausible interpretation is that this energy is dissipated as a consequence of superposition of incident and reflected waves, since nonlinear interactions generate higher modes which are more likely to dissipate. This claim is supported by laboratory (De Silva et al., 1997; Teoh et al., 1997) and numerical (Javam, 2000) experiments indicating that interactions between waves of the same frequency and wavelength cause wave-breaking through nonlinear nonresonant interactions ($k_1 \neq k_2 + k_3$), generating turbulence within the interaction region. Implications of this work may be far-reaching since M_2 internal wave dissipation often occurs at surface and bottom reflections (Nash et al., 2004; Robertson and Ffield, 2007). Other instances of locally enhanced dissipation rates following internal waves of tidal frequency emanating from steep topography occur (Lueck and Mudge, 1997; Carter et al., 2006), meaning that momentum transfer from semidiurnal waves to subinertial flow may be significant near internal tide generation sites in general. Although wave-breaking is assumed to occur via superposition, there

are other means of dissipating internal tide energy. Increasing stratification toward the surface causes the vertical wavelength and horizontal velocities to scale in a way that creates a more unstable reduced shear ($\frac{\partial u}{\partial z} - 2N > 0$). Near-surface stratification within a certain range can also cause loss of energy to solitary wave generation (da Silva et al., 2007; Gerkema, 2001).

Our principal goal is to evaluate the role of momentum transfer from semidiurnal internal tides to subinertial flow at a surface reflection north of Mendocino Escarpment. In Section 3, the equations of motion are presented and simplified. Section 4 focuses on the data processing and motivation for subsequent theoretical analysis of the momentum transfer between M_2 internal waves and the mean flow at Mendocino Escarpment. Section 5 examines the impact of dissipation, superposition and beam structure by comparing three theoretical cases. Section 6 discusses results, limitations, and broader impacts. In Section 7, the major findings are summarized.

Chapter 2

Previous Studies

Internal wave-mean momentum transfer has attracted considerable attention, particularly in the atmosphere. The mechanisms by which it occurs include critical layers, form drag, and wave-wave interactions. Each mechanism can cause wave breaking which occurs when wave amplitudes are large enough that nonlinear effects can no longer be neglected in the dynamical equations, resulting in energy transfer to other wavelengths and ultimately turbulence. Although this dissipation enables momentum transfer, the less-studied non-dissipative wave-wave interactions are also a factor. While previous literature is limited with regard to wave-wave interactions, such as the present study that examines internal tide beam surface reflection with and without dissipation, there is substantial research involving critical layers and form drag.

Critical layers, particularly in the atmosphere, are the best-studied mechanism for internal wave-mean interaction. By one definition, an internal wave encounters a critical layer when the Doppler-shifted phase speed of the wave vanishes.

Most atmospheric studies assume that the mean velocity of the wind is purely zonal and varies with height $\overline{u}(z)$ (Eliassen and Palm, 1960; Jones, 1967; Holton and Alexander, 2000). Internal gravity waves, formed by mechanisms such as airflow over rough topography (e.g., mountains), are vertically propagating waves associated with the buoyancy restoring force in a stably stratified fluid. To illustrate what happens at a critical layer, consider the simple case of a purely zonal mean flow that depends on height and an upward-propagating wave motion with a zero meridional wavenumber in an irrotational, compressible atmosphere. For this set-up, Eliassen and Palm (1960) derived a relationship involving the vertical energy-flux and momentum-flux, $\langle\widetilde{p}\widetilde{w}\rangle_x = -\rho_0(\overline{u}-c)\langle\widetilde{u}\widetilde{w}\rangle_x$ (angular brackets with subscript x represent zonal averaging, tildes represent disturbances due to internal waves, ρ_0 is constant reference buoyancy density and Boussinesq approximation holds), such that if $\overline{u}(z) \neq c$, $\rho_0\langle\widetilde{u}\widetilde{w}\rangle_x$ is independent of z. This follows because the momentum-flux is constant with height for linear, adiabatic, inviscid gravity waves, since the wave amplitude increases exponentially as air density decreases (Holton and Alexander, 2000). As the wave propagates upwards, winds are typically stronger and $\overline{u}(z) - c$ tends to zero; mountain waves yield another scenario with $c = 0$ and $\overline{u}$ tending to zero for a critical level.

Numerous atmospheric studies have examined the extent to which momentum is absorbed at a critical layer (Booker and Bretherton, 1967; Hines and Reddy, 1961; Holton and Alexander, 2000). From the dispersion relation that accompanies the above example, Holton and Alexander (2000) show that $m \approx \pm N(c-\overline{u})^{-1}$. As the wave approaches a critical layer, the vertical wavenumber tends to infinity so even a small-amplitude wave will break.

Thus, the height at which a wave breaks depends not only on its amplitude but also its vertical wavelength (smaller vertical wavelengths break lower in the atmosphere). The dissipation in this example causes momentum-flux divergences to drag the mean flow towards the phase speed of the wave, or the flow speed at the critical height.

Although a completely general theory for wave-mean flow interaction does not yet exist, the non-acceleration theorem (sometimes referred to as the non-interaction theorem) is a major step towards one. It states that given linearized, hydrostatic, harmonic waves on a spherical Earth with a zonal mean wind that is a function of latitude and pressure only, waves and mean flow do not interact in the absence of dissipation, forcing or transience (local growth or decay of wave amplitude; Boyd, 1976). Conversely, momentum is transferred to the mean flow in regions of dissipation, forcing and transience. This theory extends the work of Eliassen and Palm (1960), Charney and Drazin (1961), and Holton (1974). Complimentary studies in a Lagrangian context (Andrews and McIntyre, 1976; 1978) have also been conducted.

Consequences of momentum transfer are extremely important in the middle atmosphere. Since the 1960s, extensive research has shown that forces induced by Rossby and gravity waves are responsible for meridional transport in the stratosphere and mesosphere (Lindzen and Holton, 1968; Holton, 1980; Andrews et al., 1987; Holton and Alexander, 2000), the quasi-biennial oscillation of the zonal wind in the tropical stratosphere (Lindzen and Holton, 1968), the dampening of atmospheric winds in the stratosphere and troposphere (McFarlane, 1987), meridional transport accompanying sudden stratospheric warmings in the polar regions (mainly in the Arctic), the vertical and meridional advection of heat and trace constituents like ozone, and the ex-

istence of noctilucent clouds near the mesopause at high latitudes in the summer (Holton and Alexander, 2000).

In the ocean, wave-mean interactions associated with critical layers have been studied to a lesser degree (Jones, 1967; Bell, 1975; Muench and Kunze, 1999 and 2000). Ruddick and Joyce (1979) conducted one of the first observational studies in the ocean. They analyzed time-correlations between vertically acting Reynolds-stresses of the wave field and the mean shear from mooring data. They found significant correlations when the mean velocity was high (≈25 cm/s). Their theoretical analysis showed that momentum-fluxes lost by critical-layer absorption increased linearly with the velocity difference across the shear zone, but their data did not confirm this theoretical analysis. Another example is the equatorial deep jets, which have elevated dissipation rates in the high shear zones between jets. Muench and Kunze (1999; 2000) demonstrated the possibility that the jets are maintained by internal waves as they encounter critical layers within the jets, creating momentum-flux divergences that accelerate/decelerate the mean flow and energy-flux divergences that elevate dissipation rates; wave-wave interactions were assumed to replenish the wave spectrum.

Another mechanism (Scinocca and McFarlane, 2000; Skyllingstad and Wijesekera, 2003) is form drag, also known as pressure drag, which is associated with flow separation or topographically induced gravity waves that dissipate when the inverse Froude number F reaches a critical value F_c. The inverse Froude number is the ratio between the buoyancy frequency times the maximum topographical height and horizontal velocity, $F = Nh_0/U$. At this value, the waves become unstable and break. Simulations by Skyllingstad and Wijesekera (2003) indicate that wider obstacles have increased form drag.

In the atmosphere, winds are assumed to be constant over time and the induced waves are stationary. Parameterization schemes associated with unresolved topography that account for low-level momentum exchange originating from internal-wave breaking reduce model errors by approximately 20% (Scinocca, 2003). The scheme used by Scinocca and McFarlane (2000) reflects the inverse Froude number at the generation of the internal wave, where h_0 represents the maximum height of the subgridscale topography. The internal-wave Reynolds-stress (vertical transport of momentum) balances the form drag. When F exceeds F_c, the maximum Reynolds-stress τ_c that can continue propagating upwards is proportional to $U^3F_c^2/N$. If $F < F_c$, the wave propagates upward until it encounters a critical layer or $F = F_c$. At this point, the wave dissipates and a residual wave with Reynolds-stress τ_c continues upwards. If $F > F_c$, the wave either breaks in its first vertical wavelength due to low-level wave-breaking or vortices appear in the lee of the obstacle due to wave-blocking or flow separation, with τ_c being transported upwards. For low-level wave breaking, the parametrized rate at which momentum is deposited to the mean flow depends linearly on the form drag which is greater for ridge-like 2-D obstacles than isotropic 3-D obstacles.

Fewer studies have been conducted in the ocean for two reasons. First, high-resolution pressure measurements are more difficult to obtain, although numerical experiments provide some insight. The second complication for oceanic studies is that flow over the obstacle is usually not stationary. Theories for tidal flow over subcritical (Bell, 1975; Llewellyn-Smith and Young, 2002) and supercritical (Baines, 1982; Petrelis et al., 2006) topography have been developed. Observationally, enhanced dissipation of the barotropic tide over topography indicates that some of the energy is lost to bottom fric-

tion and the remainder to internal tides. The emanating beams are residual waves, which travel various distances before dissipating. Numerical modelling yields increasingly realistic tides and deep ocean dissipation rates if hotspots for internal tide generation are given higher dissipation values (Jayne and St. Laurent, 2001), but this improvement does not account for where the escaped waves ultimately dissipate.

A less-studied mechanism is wave-mean interactions caused by the intersections of waves (i.e., wave-wave-mean interactions). Thorpe (1997) examined internal wave reflection from a uniform slope. With resonance conditions satisfied for the incident and reflected internal waves, an alongslope flow of a few cm/s is generated in the absence of dissipation. The alongslope flow vanishes when rotation is eliminated. More recently, Thorpe (1999) theoretically determined that alongslope currents of several cm/s may be generated in a non-rotating framework when internal waves dissipate in the superposition region at a sloping boundary. He assumes that the internal waves are unaffected by molecular viscosity or nonlinear resonant interactions in the superposition region since these effects lead to nonconservation of wave frequency. In his analysis, the incident 2-D wave-field is uniform and not in a plane normal to the reflecting boundary. His research emphasizes conditions for breaking. Notably, the relationship he uses between energy-flux and momentum-flux is not applicable for a rotational system. Hence, the relationship between dissipation and momentum-flux that he derives is also not applicable. This concurs with Hogg's (1971) statement that, when dissipation is included, alongslope flows are generated by the divergence of Reynolds-stresses associated with internal waves breaking in an 'internal surf zone'. Lamb (2004) conducted a 2-D, non-hydrostatic, nonlinear numerical

simulation with internal tide beams generated at near-critical slopes. At surface reflections and where tide beams crossed, energy was lost to higher harmonic beams and mean flows with peak values of 0.6 cm/s.

Other mechanisms may exist, but have not been fully researched. One example is remote recoil, proposed by Buhler and McIntyre (2003), which occurs in the absence of any dissipation and is associated with the refraction of waves in an inhomogeneous fluid. The present study builds on our understanding of wave-wave interactions and different outcomes that result when applying initial conditions quite distinct from the most famously studied stratospheric critical layers.

Chapter 3

Theoretical Framework

In order to understand forcing of subinertial flow by internal waves, the equations of motions are examined. Simplifications motivated by the geometry and observations of the surface reflection of internal tide beams generated at Mendocino Escarpment produce a force balance in the v-momentum equation between the Coriolis term, the meridional and vertical momentum-flux divergences.

3.1 Reynolds Decomposition

The fluid is assumed to be rotating, inviscid, incompressible and Boussinesq. Since only motions with frequencies $\omega \ll N$ will be considered, the hydrostatic approximation is also made. With these simplifications, the equa-

tions of motion are

$$\frac{\partial u}{\partial t} + u\frac{\partial u}{\partial x} + v\frac{\partial u}{\partial y} + w\frac{\partial u}{\partial z} - fv = -\frac{1}{\rho_0}\frac{\partial p}{\partial x} \quad (3.1)$$

$$\frac{\partial v}{\partial t} + u\frac{\partial v}{\partial x} + v\frac{\partial v}{\partial y} + w\frac{\partial v}{\partial z} + fu = -\frac{1}{\rho_0}\frac{\partial p}{\partial y} \quad (3.2)$$

$$b = \frac{1}{\rho_0}\frac{\partial p}{\partial z} \quad (3.3)$$

$$\frac{\partial u}{\partial x} + \frac{\partial v}{\partial y} + \frac{\partial w}{\partial z} = 0 \quad (3.4)$$

$$\frac{\partial b}{\partial t} + u\frac{\partial b}{\partial x} + v\frac{\partial b}{\partial y} + w\frac{\partial b}{\partial z} + N^2 w = 0 \quad (3.5)$$

where u is the zonal velocity, v the meridional velocity, w the vertical velocity, f the Coriolis frequency (assumed constant), p the pressure anomaly, ρ_0 the reference density, $b = -\delta\rho g/\rho_0$ ($\delta\rho = \rho - \rho_0$) the buoyancy, and $N^2 = -\frac{g\partial\overline{\rho}}{\rho_0\partial z}$ the buoyancy frequency squared [$\rho = \rho_0 + \overline{\rho}(z) + \widetilde{\rho}(x, y, z, t)$, where $\overline{\rho}(z)$ is the mean density anomoly at a given depth and $\widetilde{\rho}(x, y, z, t)$ is the local perturbation density].

Using a Reynolds decomposition, each variable (e.g., u) can be separated into a mean part (e.g., $\overline{u}$), representing the subinertial flow, and perturbation part (e.g., $\widetilde{u}$) representing the internal tides. The perturbation part is sinusoidal in time. Averaging is over one wave period (denoted by $\langle\rangle_t$), the

time-mean equations of motion reduce to

$$\frac{\partial \overline{u}}{\partial t} + \nabla \cdot [\overline{u}(\overline{u}, \overline{v}, \overline{w})] + \nabla \cdot \langle \widetilde{u}(\widetilde{u}, \widetilde{v}, \widetilde{w}) \rangle_t - f\overline{v} = -\frac{1}{\rho_0}\frac{\partial \overline{p}}{\partial x} \quad (3.6)$$

$$\frac{\partial \overline{v}}{\partial t} + \nabla \cdot [\overline{v}(\overline{u}, \overline{v}, \overline{w})] + \nabla \cdot \langle \widetilde{v}(\widetilde{u}, \widetilde{v}, \widetilde{w}) \rangle_t + f\overline{u} = -\frac{1}{\rho_0}\frac{\partial \overline{p}}{\partial y} \quad (3.7)$$

$$\overline{b} = \frac{1}{\rho_0}\frac{\partial \overline{p}}{\partial z} \quad (3.8)$$

$$\frac{\partial \overline{u}}{\partial x} + \frac{\partial \overline{v}}{\partial y} + \frac{\partial \overline{w}}{\partial z} = 0 \quad (3.9)$$

$$\frac{\partial \overline{b}}{\partial t} + \nabla_H \cdot [\overline{b}(\overline{u}, \overline{v})] + \nabla_H \cdot \langle \widetilde{b}(\widetilde{u}, \widetilde{v}) \rangle_t + \overline{w}\overline{N}^2 = 0. \quad (3.10)$$

The $\frac{\partial}{\partial t}$ terms represent accelerations which operate on time-scales much longer than the semidiurnal period. The perturbation parts appear in nonlinear terms of the time-mean equations of motion. The momentum equations include forcings due to the time-mean internal wave momentum-flux divergences. The mean buoyancy equation was simplified using continuity and the fact that b and w are 90° out of phase for linear internal gravity waves. The forcing in the buoyancy equation is the remaining time-mean internal wave buoyancy-flux divergence.

3.2 Consistency Relations between $\widetilde{u}$, $\widetilde{v}$, $\widetilde{w}$ and $\widetilde{b}$

Relationships between $\widetilde{u}$, $\widetilde{v}$ and $\widetilde{w}$ can be derived from the linearized perturbation equations

$$\frac{\partial \widetilde{u}}{\partial t} - f\widetilde{v} = -\frac{1}{\rho}\frac{\partial \widetilde{p}}{\partial x} \tag{3.11}$$

$$\frac{\partial \widetilde{v}}{\partial t} + f\widetilde{u} = -\frac{1}{\rho}\frac{\partial \widetilde{p}}{\partial y} \tag{3.12}$$

$$\widetilde{b} = \frac{1}{\rho_0}\frac{\partial \widetilde{p}}{\partial z} \tag{3.13}$$

$$\frac{\partial \widetilde{u}}{\partial x} + \frac{\partial \widetilde{v}}{\partial y} + \frac{\partial \widetilde{w}}{\partial z} = 0. \tag{3.14}$$

Taking the derivative with respect to y of the u-momentum equation (3.11) and with respect to x of the v-momentum equation (3.12), then combining gives

$$\frac{\partial}{\partial t}\left(\frac{\partial \widetilde{u}}{\partial y} - \frac{\partial \widetilde{v}}{\partial x}\right) = f\left(\frac{\partial \widetilde{u}}{\partial x} + \frac{\partial \widetilde{v}}{\partial y}\right). \tag{3.15}$$

Assuming a solution of the form $\exp\left[i(kx + ly + mz - \omega t)\right]$,

$$\widetilde{v} = -\frac{(fik - \omega l)}{(fil + \omega k)}\widetilde{u} = \frac{lk(\omega^2 - f^2) - if\omega(l^2 + k^2)}{f^2l^2 + \omega^2k^2}\widetilde{u}. \tag{3.16}$$

Using continuity (3.14) and (3.16) yields a relationship between $\widetilde{w}$ and $\widetilde{u}$

$$\widetilde{w} = \frac{-(k\widetilde{u} + l\widetilde{v})}{m} = \frac{-\omega^2k(l^2 + k^2) + if\omega l(l^2 + k^2)}{m(f^2l^2 + \omega^2k^2)}\widetilde{u}. \tag{3.17}$$

Relations (3.16) and (3.17) are consistent with Frankignoul (1974). The perturbation buoyancy expressed in terms of $\widetilde{v}$ is

$$\widetilde{b} = \left\{ \frac{fm}{k} \left[1 - \frac{\omega^2(l^2+k^2)}{f^2k^2+\omega^2l^2} \right] + i \left[\frac{lm\omega(\omega^2-f^2)}{f^2k^2+\omega^2l^2} \right] \right\} \widetilde{v}. \tag{3.18}$$

3.3 Simplifying the Equations of Motion

To simplify the analysis, consider the 2-D situation without any variation in the zonal x-direction (i.e., $\frac{\partial}{\partial x} = k = 0$). We concentrate on the situation with rotation, but the irrotational setting is also briefly presented to demonstrate differences in dynamics near the equator.

3.3.1 With Rotation

With the additional 2-D assumption, the equations of motion (3.1) - (3.5) reduce to

$$\begin{aligned}
\frac{\partial u}{\partial t} + v\frac{\partial u}{\partial y} + w\frac{\partial u}{\partial z} - fv &= 0 && (3.19)\\
\frac{\partial v}{\partial t} + v\frac{\partial v}{\partial y} + w\frac{\partial v}{\partial z} + fu &= -\frac{1}{\rho_0}\frac{\partial p}{\partial y} && (3.20)\\
b &= \frac{1}{\rho_0}\frac{\partial p}{\partial z} && (3.21)\\
\frac{\partial v}{\partial y} + \frac{\partial w}{\partial z} &= 0 && (3.22)\\
\frac{\partial b}{\partial t} + v\frac{\partial b}{\partial y} + w\frac{\partial b}{\partial z} + N^2 w &= 0. && (3.23)
\end{aligned}$$

Reynolds decomposition yields the mean equations of motion without zonal gradients

$$\frac{\partial \overline{u}}{\partial t} + \left(\frac{\partial}{\partial y}, \frac{\partial}{\partial z}\right) \cdot [\overline{u}(\overline{v}, \overline{w}) + \langle \widetilde{u}(\widetilde{v}, \widetilde{w})\rangle_t] - f\overline{v} = 0 \tag{3.24}$$

$$\frac{\partial \overline{v}}{\partial t} + \left(\frac{\partial}{\partial y}, \frac{\partial}{\partial z}\right) \cdot [\overline{v}(\overline{v}, \overline{w}) + \langle \widetilde{v}(\widetilde{v}, \widetilde{w})\rangle_t] + f\overline{u} = -\frac{1}{\rho_0}\frac{\partial \overline{p}}{\partial y} \tag{3.25}$$

$$\overline{b} = \frac{1}{\rho_0}\frac{\partial \overline{p}}{\partial z} \tag{3.26}$$

$$\frac{\partial \overline{v}}{\partial y} + \frac{\partial \overline{w}}{\partial z} = 0 \tag{3.27}$$

$$\frac{\partial \overline{b}}{\partial t} + \frac{\partial}{\partial y}\overline{b}\overline{v} + \frac{\partial}{\partial y}\langle \widetilde{b}\widetilde{v}\rangle_t + \overline{w}\overline{N}^2 = 0. \tag{3.28}$$

Again, $\langle \widetilde{w}\widetilde{b}\rangle_t = 0$ since the vertical velocity perturbation and density perturbations are out of phase for linear internal waves.

The phase relationships in the $k = 0$ case yield

$$\widetilde{v} = -i\frac{\omega}{f}\widetilde{u} \tag{3.29}$$

$$\widetilde{w} = i\frac{l\omega}{mf}\widetilde{u} \tag{3.30}$$

$$\widetilde{b} = \frac{\omega^2 m}{fl}\left(1 - \frac{f^2}{\omega^2}\right)\widetilde{u} \tag{3.31}$$

which further simplifies subinertial u-momentum conservation (3.24) and buoyancy conservation (3.28)

$$\frac{\partial \overline{u}}{\partial t} + \left(\frac{\partial}{\partial y}, \frac{\partial}{\partial z}\right) \cdot \overline{u}(\overline{v}, \overline{w}) - f\overline{v} = 0 \tag{3.32}$$

$$\frac{\partial \overline{b}}{\partial t} + \frac{\partial}{\partial y}\overline{b}\overline{v} + \overline{w}\overline{N}^2 = 0. \tag{3.33}$$

If $\overline{u}$ changes slowly over time such that $\frac{\partial \overline{u}}{\partial t} \approx 0$ and the momentum-flux divergences in the u-momentum equation (3.32) are negligible, then (3.32) implies that $\overline{v}$ is small. In this case, the steady equations are

$$
\begin{aligned}
f\overline{v} &= 0 && (3.34)\\
\left\langle \left(\frac{\partial}{\partial y}, \frac{\partial}{\partial z} \right) \cdot \widetilde{v}(\widetilde{v}, \widetilde{w}) \right\rangle_t + f\overline{u} &= -\frac{1}{\rho_0} \frac{\partial \overline{p}}{\partial y} && (3.35)\\
\overline{b} &= \frac{1}{\rho_0} \frac{\partial \overline{p}}{\partial z} && (3.36)\\
\frac{\partial \overline{w}}{\partial z} &= 0 && (3.37)\\
\overline{w}\overline{N}^2 &= 0. && (3.38)
\end{aligned}
$$

Thus, $\overline{w}$ is constant over depth, so must be zero everywhere due to boundary conditions at the surface and ocean floor. Hence, $\overline{b}$ is constant over time everywhere. The force balance in the v-momentum equation (3.35) is between the Reynolds-stress divergences, the Coriolis force and the pressure gradient. Assuming that there is no initial meridional pressure gradient, then a pressure gradient can never develop if $\overline{v} = \overline{w} = 0$. Thus, v-momentum equation (3.35) reduces to

$$
f\overline{u} = -\left\langle \left(\frac{\partial}{\partial y}, \frac{\partial}{\partial z} \right) \cdot \widetilde{v}(\widetilde{v}, \widetilde{w}) \right\rangle_t . \tag{3.39}
$$

This Ekman-like force balance between the Coriolis force and momentum-flux divergences will be the primary means for analyzing the extent to which internal tides drive subinertial flow at Mendocino Escarpment.

3.3.2 Without Rotation

If $f = 0$, the consistency relations are $\widetilde{u} = 0$, $\widetilde{w} = -\frac{l}{m}\widetilde{v}$ and $\widetilde{b} = i\frac{\omega m}{l}\widetilde{v}$. The time-mean equations (3.24) - (3.28) become

$$\frac{\partial \overline{u}}{\partial t} + \left(\frac{\partial}{\partial y}, \frac{\partial}{\partial z}\right) \cdot \overline{u}(\overline{v}, \overline{w}) = 0 \tag{3.40}$$

$$\frac{\partial \overline{v}}{\partial t} + \left(\frac{\partial}{\partial y}, \frac{\partial}{\partial z}\right) \cdot [\overline{v}(\overline{v}, \overline{w}) + \langle \widetilde{v}(\widetilde{v}, \widetilde{w})\rangle_t] = -\frac{1}{\rho_0}\frac{\partial \overline{p}}{\partial y} \tag{3.41}$$

$$\overline{b} = \frac{1}{\rho_0}\frac{\partial \overline{p}}{\partial z} \tag{3.42}$$

$$\frac{\partial \overline{v}}{\partial y} + \frac{\partial \overline{w}}{\partial z} = 0 \tag{3.43}$$

$$\frac{\partial \overline{b}}{\partial t} + \frac{\partial}{\partial y}\overline{b}\overline{v} + \overline{w}\overline{N}^2 = 0. \tag{3.44}$$

In comparison with the rotating case, if $\overline{u}$ changes slowly over time and the momentum-flux divergence in the u-momentum equation (3.40) is negligible, then (3.40) does not provide information about $\overline{v}$. From (3.41), internal wave momentum-flux divergence can accelerate the meridional velocity until it creates a balancing meridional pressure gradient. When this balancing is achieved, the meridional gradient of buoyancy is the negation of the depth gradient of internal wave momentum-flux divergences [combining (3.41) and the meridional gradient of (3.41)].

Chapter 4

Mendocino Escarpment Data Analysis

The purpose of this section is to examine a setting in which the momentum-flux of an internal tide beam is diminished after its first surface reflection, motivating further examination of potential contributions to the mean flow in the dissipation region. To do so requires a description of the data and its collection site, isolation of the semidiurnal internal tide, calculations of the energy- and momentum-fluxes, and a comprehensive interpretation.

4.1 Data

From September 25 to October 22, 1997, full-depth profiles of horizontal velocities (u, v), pressure, temperature, and salinity measurements were collected using the Absolute Velocity Profiler (AVP; Sanford et al., 1985) at Mendocino Escarpment (Althaus et al. 2003). This site is a zonal transform fault at approximately 40° 20′ N, west of northern California. Its flanks are

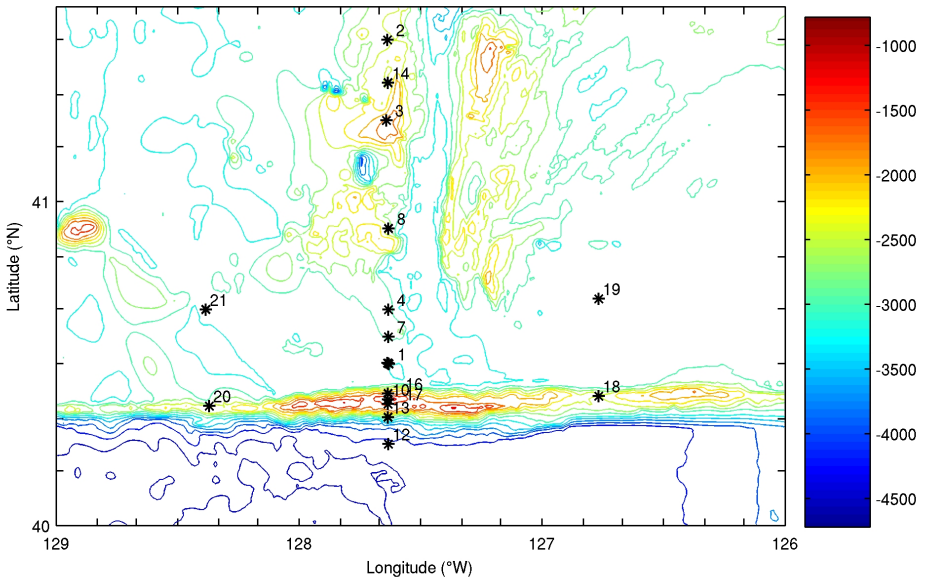

Figure 4.1: Asterisks indicate a) main transect stations with at least four profiles and b) stations at latitudes to the east and west of the main transect. Bathymetry is taken from Smith and Sandwell (1997). The bathymetry contour interval is 250 m.

supercritical for semidiurnal internal waves. It is oriented perpendicular to the impinging semidiurnal barotropic tidal currents which take the form of coastally-trapped poleward-propagating Kelvin waves.

Each station was occupied for 12-15 hours to isolate the 12.4-hour semidiurnal signal. Twelve stations (Figure 4.1) along the main transect (127° 38′ W) are suitable for isolating the semidiurnal tide because they include at least four profiles. This analysis concentrates on downcast data only. As this transect is aligned perpendicular to the ridge, an internal tide generated at the ridge should propagate north and south through the transect stations (neglecting zonal variability). This motivates a 2-D (y, z) interpretation. Four stations (Figure 4.1) to the east and west are used to examine zonal dependence. All station numbers, locations, date, time, and number of drops

are listed sequentially in Table 4.1. Lowercase letters on the station numbers indicate that the station was revisited at a later time. Major phases of the moon over this time period are shown in Table 4.2. For a more thorough description of the data, see Althaus et al. (2003).

4.2 Data Processing and Analysis

To study internal tides involves quantifying numerous physical variables and utilizing multiple techniques. Pertinent physical variables include isopycnal displacements, velocities, energy-fluxes and momentum-fluxes. Techniques include WKB-scaling, least-squares sinusoidal fitting and ray theory.

Althaus et al. (2003) demonstrated that semidiurnal internal tides are generated at the ridge. They inferred high turbulent dissipation rates (greater than 10^{-8} W/kg) accompanied by a baroclinic energy-flux drop from about 4 to 2 kW/m near the first surface reflection of the northward beam. Consequently, the focus will be on this region, but the entire main transect is examined to justify this interpretation. First, isopycnal displacements, velocities and energy-fluxes are calculated similarly to Althaus et al. (2003). These derivations and resulting values are compared. Finally, internal tide momentum-fluxes are assessed, motivating subsequent theoretical analysis.

4.2.1 Isopycnal Displacement

Following Desaubies and Gregg (1981), isopycnal displacements $\widetilde{\xi}(z,t)$ are inferred by subtracting the mean depth from the instantaneous depth of

Table 4.1: Station Details

Station	Latitude (N)	Longitude (W)	UTC Date & Time	Profiles
1a	40° 29.97′	127° 37.76′	26-Sep-1997 11:20:33	5
2	41° 29.88′	127° 38.16′	27-Sep-1997 13:06:26	5
3	41° 14.99′	127° 38.44′	28-Sep-1997 11:35:17	7
1b	40° 30.06′	127° 37.98′	9-Sep-1997 11:04:36	5
4	40° 39.97′	127° 37.87′	30-Sep-1997 11:09:50	6
5	40° 55.26′	127° 38.75′	01-Oct-1997 19:17:40	1
6a	39° 54.96′	127° 38.51′	02-Oct-1997 14:16:20	3
7	40° 34.95′	127° 37.97′	03-Oct-1997 11:26:09	6
8	40° 55.02′	127° 37.89′	04-Oct-1997 11:30:30	6
1c	40° 30.11′	127° 38.16′	05-Oct-1997 00:16:36	5
9	40° 9.89′	127° 38.11′	05-Oct-1997 23:44:16	1
10a	40° 23.33′	127° 37.99′	06-Oct-1997 11:04:50	8
6b	39° 55.04′	127° 37.87′	08-Oct-1997 11:10:28	3
11	39° 35.04′	127° 37.92′	09-Oct-1997 16:04:20	2
12	40° 15.13′	127° 37.96′	12-Oct-1997 11:24:48	4
13	40° 20.09′	127° 38.01′	13-Oct-1997 11:15:43	5
14	41° 21.98′	127° 38.02′	14-Oct-1997 11:09:15	6
10b	40° 23.35′	127° 37.99′	15-Oct-1997 11:25:10	9
18	40° 23.99′	126° 46.00′	16-Oct-1997 11:18:50	4
19	40° 41.98′	126° 45.99′	17-Oct-1997 13:07:25	1
20	40° 22.15′	128° 22.15′	18-Oct-1997 16:06:08	4
21	40° 40.03′	128° 23.01′	19-Oct-1997 11:23:10	4
15	40° 26.01′	127° 38.01′	20-Oct-1997 15:24:09	3
16	40° 24.50′	127° 38.01′	21-Oct-1997 14:06:40	6
17	40° 22.50′	127° 38.00′	22-Oct-1997 14:10:20	6

Table 4.2: Moon Phases

Phase	UTC Date & Time
Last Quarter	23-Sep-1997 13:35
New Moon	1-Oct-1997 16:52
First Quarter	9-Oct-1997 12:22
Full Moon	16-Oct-1997 03:46
Last Quarter	23-Oct-1997 04:48

a particular isopycnal

$$\widetilde{\xi}(z,t) \;=\; z(\sigma_\theta,t) \;-\langle z(\sigma_\theta)\rangle_t \tag{4.1}$$

where σ_θ is potential density.

Figure 4.2 shows isopycnal displacement profile pairs at Stations 1 and 10, each pair taken nearly half a semidiurnal period apart. Station 1 is located about 0.1° north of the ridge, while Station 10 is located closest to the ridge crest. The near mirror-imaging at some depths demonstrates the dominance of the M_2 frequency.

4.2.2 Smoothing

To smooth the profiles, data were segmented into 10 m overlapping windows and an average of the values in each segment taken. The squared buoyancy frequency was smoothed over 100 m intervals. In 36 out of over 29,000 intervals where calculations yielded negative squared buoyancy frequencies, values were reset to 1×10^{-8} rad/s which is less than the semidiurnal frequency. After smoothing, there are 41 intervals where $N < M_2$, but these are always near the ocean floor. Thus, it is assumed that propagation of the internal tides is unaffected (i.e., $f < M_2 < N$).

4.2.3 Barotropic and Baroclinic Velocities

The barotropic velocity field is due to pressure gradients induced by sloping sea surface heights and is independent of depth except to the extent that it is influenced by bottom friction. Barotropic horizontal velocities were obtained from smoothed data by taking the depth-average of the full-depth

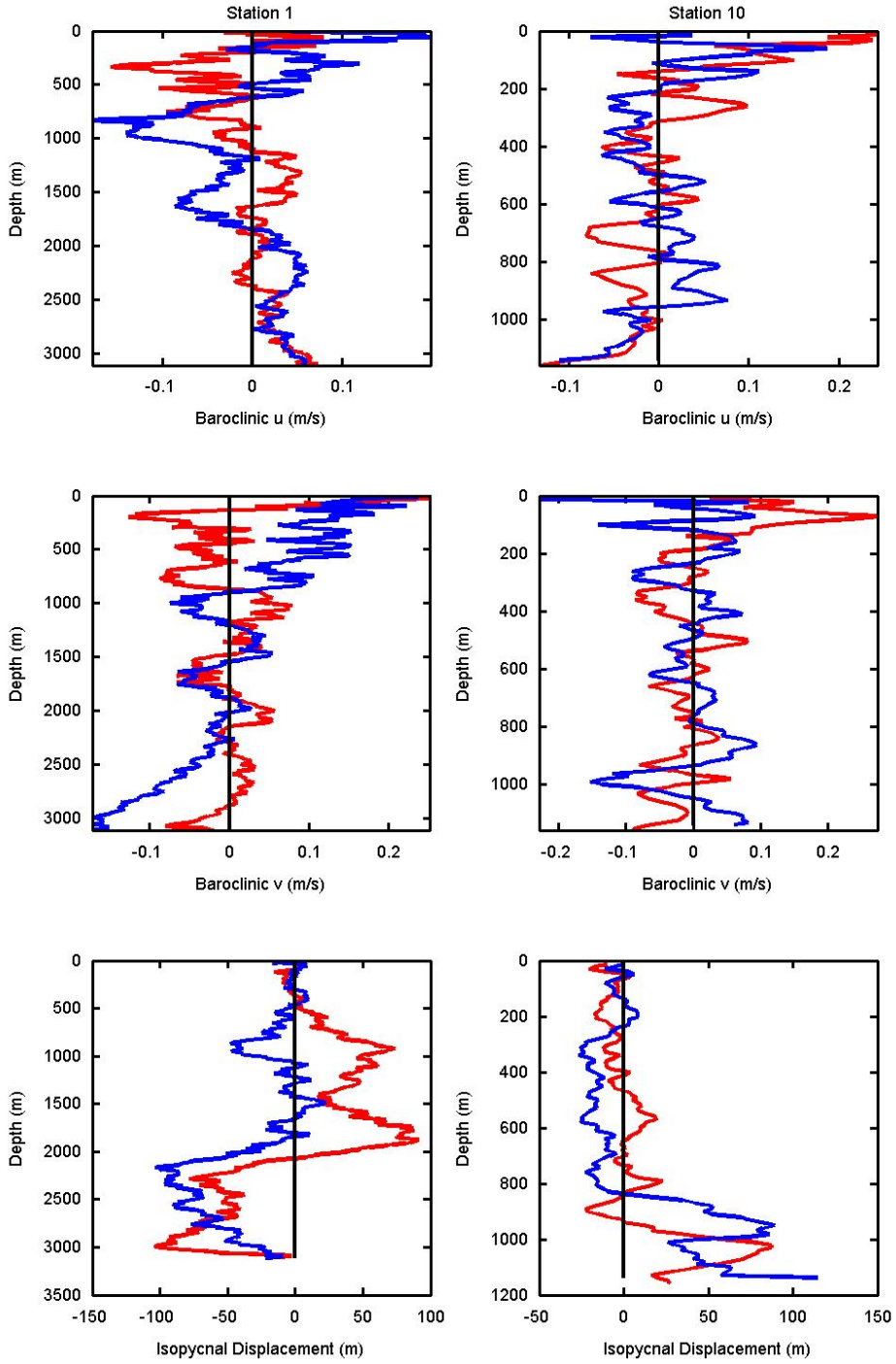

Figure 4.2: Horizontal baroclinic velocities $(\widetilde{u}, \widetilde{v})$ and isopycnal displacements versus depth at Stations 1 and 10. Red and blue curves are approximately 6.2 hours apart. Station 1 is located about 0.1° north of the ridge, while Station 10 is located closest to the ridge crest.

profiles. Averaging over all 115 profiles, the mean barotropic meridional (zonal) velocity is 0.012 m/s (0.008 m/s), with a standard deviation of 0.034 m/s (0.03 m/s). Althaus et al. (2003) demonstrated that the measured meridional barotropic velocities fit to a sinusoid at the semidiurnal frequency agreed with TPXO.3 model tidal predictions.

Baroclinic velocities were obtained by subtracting the barotropic part from the smoothed velocity profiles. Figure 4.2 illustrates the dominant semidiurnal frequency, showing profiles taken approximately 6.2 hours apart for Stations 1 and 10.

4.2.4 WKB-Scaling

The purpose of WKB-scaling is to remove the effect of changing stratification with depth. It stretches out layers of intense stratification and compresses layers of low stratification. It eliminates surface intensification of the horizontal velocities, and the bottom intensification of the isopycnal displacements and vertical velocity. This approximation is valid when $N(z)$ varies slowly over the vertical wavelength $2\pi/m$.

WKB-scaled horizontal velocities, vertical displacements, and depth coordinates are defined as in Althaus et al. (2003), although the reference buoyancy frequency differs. Since the reference buoyancy frequency in this study is $N_{ref} = 0.0052\ rad/s$, some discrepancies may exist with Althaus et al. (2003) who used $N_{ref} = 0.0025\ rad/s$.

4.2.5 Least-Squares Sinusoidal Fits

For each station with at least four profiles, a least-squares sinusoidal fit to the semidiurnal frequency is made at each depth, such that $u_i(z) = u_0(z) + u_s(z)\sin(-M_2 t_i) + u_C(z)\cos(-M_2 t_i) + \epsilon_i, i = 1 : n$ where n is the number of drops at a particular station. This can be rearranged as:

$$\begin{aligned} U(z) &= \begin{pmatrix} 1 & \sin(-M_2 t_1) & \cos(-M_2 t_1) \\ 1 & \sin(-M_2 t_2) & \cos(-M_2 t_2) \\ \vdots & \vdots & \vdots \\ 1 & \sin(-M_2 t_n) & \cos(-M_2 t_n) \end{pmatrix} \begin{pmatrix} U_0 \\ U_S \\ U_C \end{pmatrix} + \epsilon \\ &= AU_{coeffs} + \epsilon \end{aligned} \tag{4.2}$$

where ϵ is the residual vector. The total error is expressed as $||\epsilon||^2 = ||U - AU_{coeffs}||^2$. Similar fits were done for meridional velocity and vertical displacement. When using a zero time-mean for the vertical displacement, the residuals were systematically biased since isopycnal displacements are relative to $\langle z(\sigma_\theta)\rangle_t$ (averaged over all stations). Since repeating the exercise with a non-zero time-mean reduced the error, this version is used for subsequent derivations. The semidiurnal vertical velocity was obtained by taking the time-derivative of vertical displacement. An example of the least-squares fit is shown in Figure 4.3 for Station 4, at a depth of approximately 1000 m.

To establish the goodness of the sinusoidal fits, the total squared residual was divided by the rms of the data for each depth (i.e. $\sum \epsilon_i^2 / \sum u_i^2$). The station averages of the goodness of fit range from 1.1 to 9.2% for zonal velocity, 0.8 to 3.6% for meridional velocity and 0.4 to 8.6% for the isopycnal

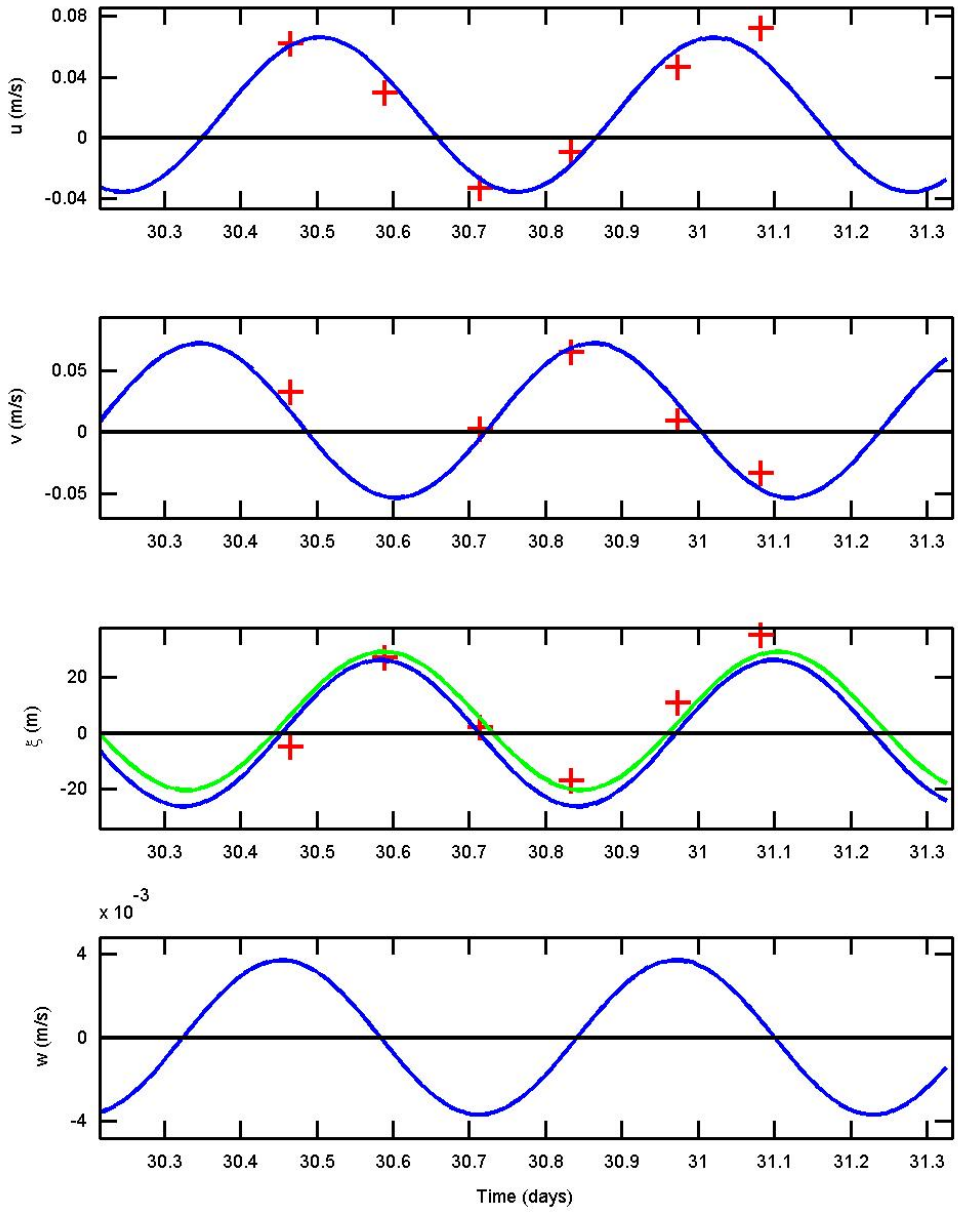

Figure 4.3: Sinusoidal fits of horizontal velocities $(\widetilde{u}, \widetilde{v})$, isopycnal displacement, and resulting semidiurnal vertical velocity for Station 4 at a depth of approximately 1000 m. Actual data points are denoted by +'s. For isopycnal displacements, the blue curve corresponds to calculations obtained by setting the time-mean isopycnal displacement to zero, while the green curve allows for a non-zero time-mean.

displacements. The most obvious explanation for residual error is internal waves at other frequencies. If $\epsilon_i^2/u_i^2 > 1$, the fit was considered erroneous and not used in subsequent analysis.

4.2.6 Amplitude and Phase

From the coefficients in the least-squares fits, the amplitude, A, and phase, ϕ, of the horizontal baroclinic velocities and isopycnal displacements were obtained.

$$A = \sqrt{u_C^2 + u_S^2} \tag{4.3}$$

$$\phi = -\arctan(u_S/u_C). \tag{4.4}$$

This follows from $u_i(z) = u_0(z) + A\cos(-M_2 t_i - \phi), i = 1, \ldots, n$.

The WKB-scaled amplitudes and phases for isopycnal displacements, zonal and meridional velocities from Station 4, approximately 33 km north of the ridge, are shown in Figure 4.4. Compared to Figure 5 in Althaus et al. (2003), the difference in the chosen reference buoyancy frequency accounts for relatively decreased WKB-scaled isopycnal displacement amplitudes and relatively increased WKB-scaled horizontal velocities. Taking this into account, the amplitudes and phases support results from Althaus et al. (2003). Scaled isopycnal displacements are approximately 10-20 m and horizontal velocity amplitudes approximately 0.1 m/s, with meridional amplitudes slightly higher than zonal amplitudes. Phases increase with depth, implying upward energy propagation (LeBlond and Mysak, 1978). Generally, it was difficult to discern a clear trend in phase propagation at each station but, since our efforts focus on a narrow beam path, this is not a concern.

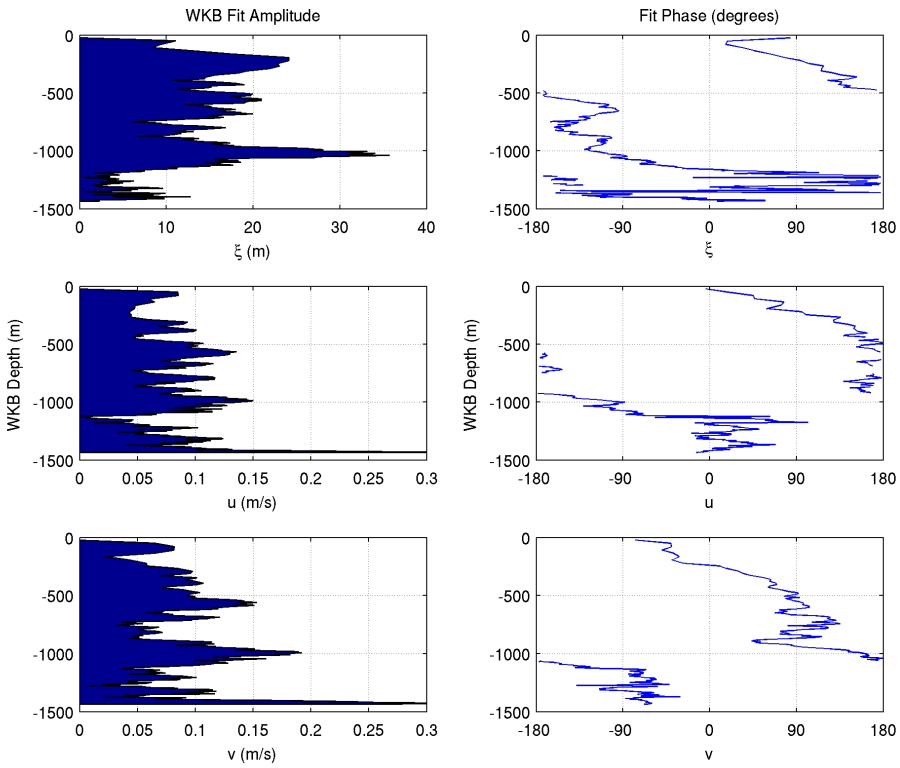

Figure 4.4: WKB-scaled amplitudes and phase for isopycnal displacements, zonal and meridional internal tide velocities at Station 4.

4.2.7 Internal Tide Beam

The energy of a freely propagating internal wave travels with slope

$$s_{\pm} = \pm\frac{\sqrt{k^2 + l^2}}{m} = \pm\sqrt{\frac{\omega^2 - f^2}{N^2 - \omega^2}} \tag{4.5}$$

which simplifies to $s_{\pm} = \pm\frac{l}{m}$ when $k = 0$. This ray-tracing technique requires that $N(z)$ varies slowly over the vertical wavelength $2\pi/m$ such that the WKB-approximation holds (Gill, 1982). An f-plane model is used with latitude 40° 22', corresponding to Coriolis frequency $f = 9.42 \times 10^{-5}$ rad/s = 8.14 rad/day (18.5 hours). The frequency of the M_2 (12.4 hours) semidiurnal internal tides is $\omega = M_2 = 1.41 \times 10^{-4}$ rad/s = 12.16 rad/day. The buoyancy frequency at each depth is averaged over all profiles. When WKB-scaling, the reference buoyancy frequency $N_{ref} = 0.0052$ rad/s, implying the slope $s_{\pm} = \pm 0.02$.

Topographical slopes are critical when equal to the slope of the internal wave. Generation of an internal tide beam occurs due to blocking at sites with convex topography that switches from sub- to supercritical (Garrett and Kunze, 2007). Using bathymetry from Smith and Sandwell (1997), the topographical slope along the main transect is shown in Figure 4.5a, with the internal tide slope plotted for reference. Corresponding ray paths emanating from the ridge are shown (Figure 4.5b). Vertical lines denote stations bracketing the first surface reflection.

The baroclinic energy density in the semidiurnal sinusoidal fits (Althaus et al, 2003) is enhanced along ray paths emanating north from the ridge crest. The concentration of baroclinic energy in this narrow region is referred to as a beam. Beams are characteristic features of internal tides (Vlasenko et

al., 2005; Pingree and New, 1991; Holloway and Merrifield, 1999; Gerkema et al., 2004) that form at near-critical slopes.

4.2.8 Energy-Flux

Baroclinic energy density flux is the product of the baroclinic pressure anomaly and perturbation velocity $\boldsymbol{F_E}=\boldsymbol{c_g}E = <\widetilde{\boldsymbol{u}}\widetilde{p}>_t$, where

$$\begin{aligned} \widetilde{p}(z,t) &= p_{surf}(t) + \int_z^0 \widetilde{\rho}(z,t) g d\widehat{z} \\ &= -\frac{1}{H}\int_{-H}^0 \int_z^0 \widetilde{\rho}(z,t) g d\widehat{z} dz + \int_z^0 \widetilde{\rho}(z,t) g d\widehat{z}, \end{aligned} \tag{4.6}$$

since the depth average of the baroclinic pressure perturbation is zero (Kunze et al., 2002). The density anomaly is defined in terms of vertical displacement of an isopycnal, $\widetilde{\rho}(z,t) = \frac{\overline{\rho(z)}}{g}\overline{N}^2(z)\xi(z,t)$. Like Althaus et al. (2003), $\overline{\rho(z)}$ is approximated using reference density, ρ_0, and energy-flux is determined from semidiurnal fits.

To compare with results from Althaus et al. (2003; Figure 8), WKB meridional energy-flux versus depth for Station 4, approximately 33 km north of the ridge, is shown in Figure 4.6. The structure is very similar, although smaller-scale features differ slightly as a consequence of using slightly different semidiurnal fitting frequencies. Since the reference buoyancy frequency used in the WKB-scaling is twice as large as in Althaus et al. (2003), energy-fluxes are also twice as large.

WKB-scaled meridional and vertical energy-fluxes for all main transect stations (Figure 4.7) are often parallel to the ray path and enhanced in beam-like structures emanating from the ridge. For the upward- and northward-propagating beam, fluxes are greatest near the surface reflection. There is

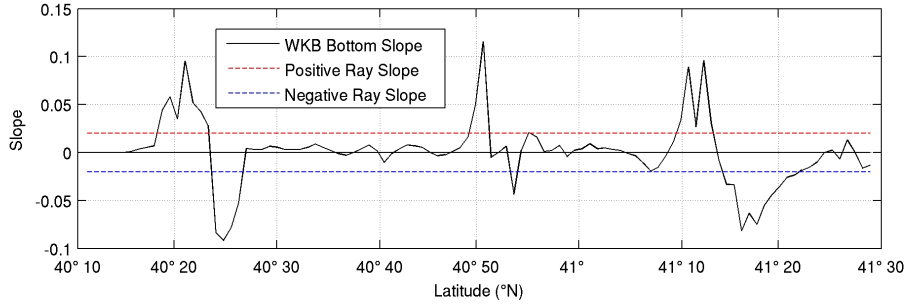

(a)

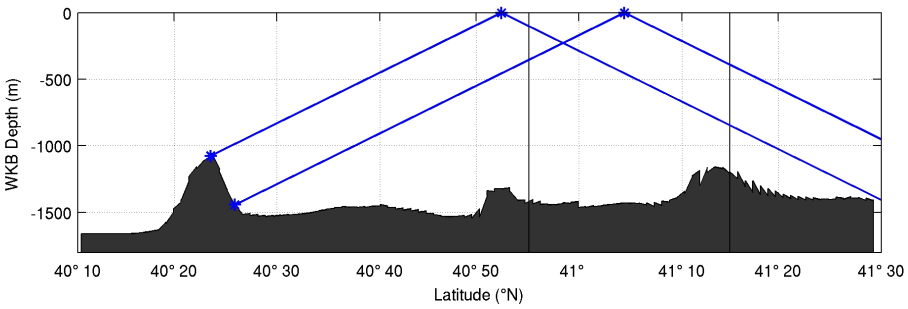

(b)

Figure 4.5: Critical slopes along the main transect are evident in a) where the topographical slope is plotted versus latitude. The two horizontal lines represent the positive and negative slopes for semidiurnal ray paths. In b), sample semidiurnal ray paths are shown emanating from Mendocino Escarpment at critical slopes and reflecting off the surface. Vertical lines indicate the profiles perceived to be immediately before the first surface reflection (Station 8) and the following profile (Station 3). Bathymetry is taken from longitudes encompassing the main transect from 124 to 130°W (Smith and Sandwell, 1997). A wider range of longitudes is used here than in subsequent figures to enable better latitudinal resolution for topographical slopes.

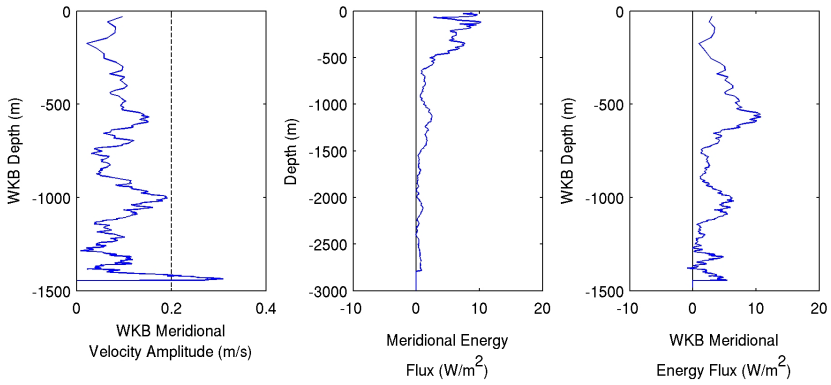

Figure 4.6: The a) WKB meridional velocity amplitude, b) meridional energy-flux, and c) WKB meridional energy-flux are plotted versus depth for Station 4, approximately 33 km north of the ridge.

some flattening (the ratio of the vertical to meridional energy-flux decreases) which indicates superposition with a downward beam, possibly with its own surface reflection. The subsequent station (Station 3) shows a downward energy-flux consistent with a surface reflection. For the most part, our fluxes concur with Althaus et al. (2003). Notable exceptions are at Stations 3, 7 and 10. For Station 3, the flux is in the opposite direction along the ray path of the surface-reflected beam. At Station 7, our fluxes are much more bottom-intensified and in the opposite direction in the abyss. Bottom intensification seems physically realistic, since it could be associated with reflection of a downward, northward beam emanating from the ridge. At Station 10, energy-flux is enhanced, particularly at the bottom. This large energy-flux is consistent with internal tide generation near the ridge crest.

The WKB-scaled zonal energy-fluxes (Figure 4.8) demonstrate substantial eastward flux south of the ridge and near the bottom at Station 4. Smaller westward fluxes contribute to the northward beam, but to a much lesser degree than the meridional fluxes. These general directions accord with the

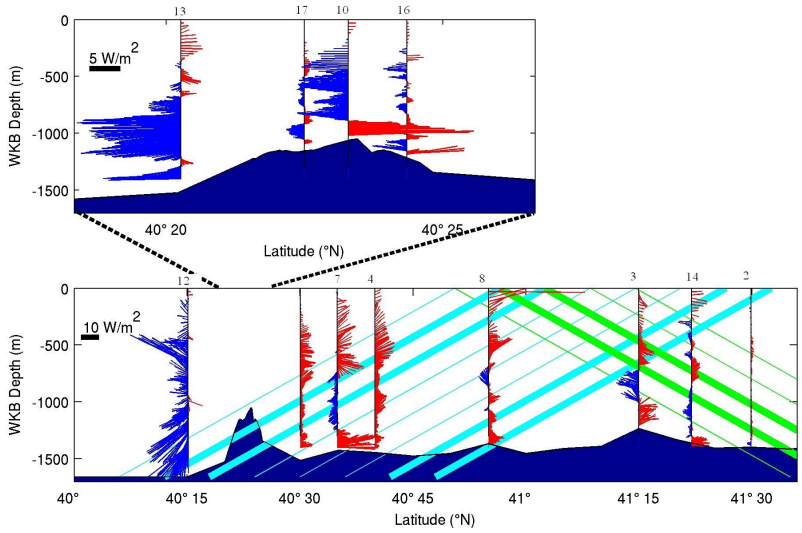

Figure 4.7: WKB-scaled meridional and vertical baroclinic energy-fluxes from the semidiurnal fits for main transect stations with a minimum of 4 profiles. Northward fluxes are red, southward blue. Ray paths are drawn to show energy propagation of the semidiurnal wave (not shown in upper panel since scaling causes them to appear horizontal). The blue represents upgoing rays and green represents downgoing rays; thicker lines indicate ray paths that would converge on Station 3.

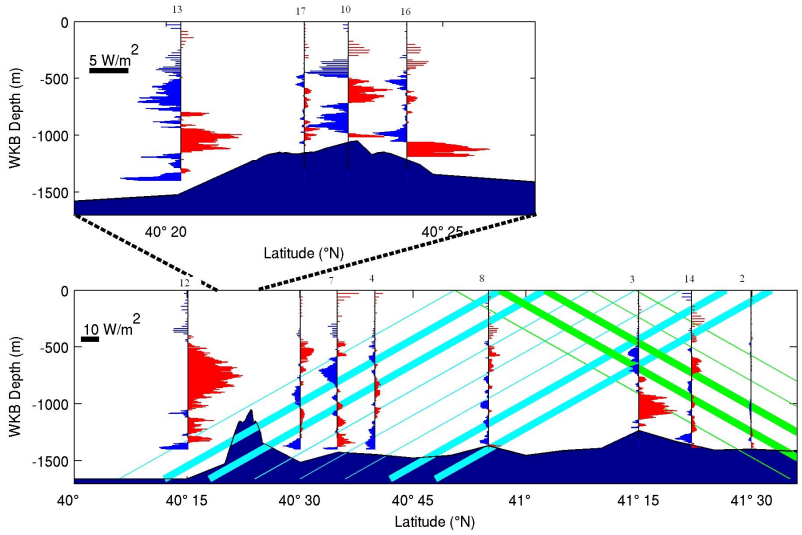

Figure 4.8: WKB-scaled zonal energy-fluxes from the semidiurnal fits for main transect stations with a minimum of 4 profiles. Eastward fluxes are red, westward blue. Ray paths are drawn to show energy propagation of the semidiurnal wave (not shown in upper panel since scaling causes them to appear horizontal). The blue represents upgoing rays and green represents downgoing rays; thicker lines indicate ray paths that would converge on Station 3.

depth-integrated horizontal energy-fluxes (Althaus et al., 2003), but specific differences occur at Stations 7 and 8. There is comparably less zonal flux near the surface reflection (Station 8) and opposing zonal flux in the bottom half of Station 7 (as in the vertical and meridional directions).

Ratios between vertical and horizontal (vertical and meridional) energy-fluxes at each depth and for each station along the main transect are shown in Figure 4.9 by the blue (red) curves. First, consider the curves in relation to the ray-path slope for a semidiurnal internal wave ($s = 0.02$), since ratios near s indicate a beamlike structure. Ratios less (greater) than s indicate contributions from upward and downward (northward and southward) propagating waves. Second, the two curves are compared. Since the curves usually

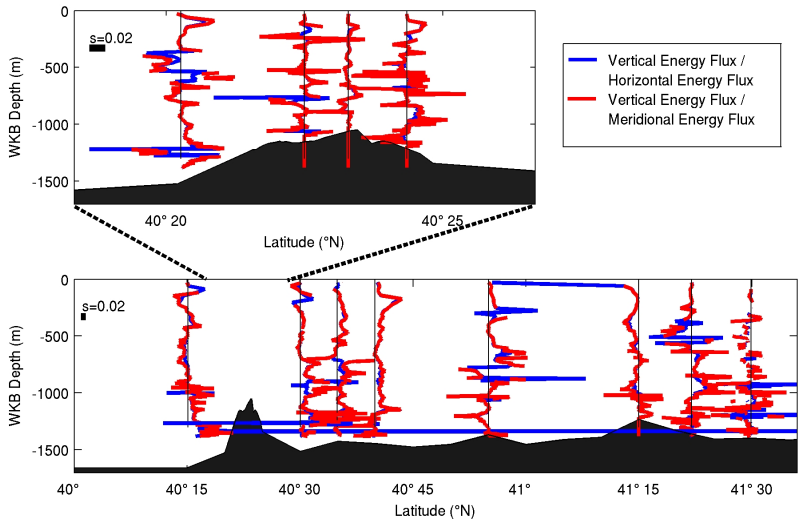

Figure 4.9: WKB-scaled energy-flux ratios from the semidiurnal fits for main transect stations with a minimum of 4 profiles. The ratio of vertical to horizontal energy-flux is blue, vertical to meridional is red (where only values less than 0.2 were plotted to avoid singularities).

overlap, meridional energy-flux dominates in the horizontal-plane and the assumption that $\frac{\partial}{\partial x} = 0$ holds.

A study by Nash et al. (2005) assessed the error involved in calculating the semidiurnal energy-flux from a regularly sampled time-series based on parameters at the Hawaiian Ridge (21-25° N). Their study indicates that, if the wavefield is dominated by semidiurnal variance, four data points over the semidiurnal period (12.4 hours) can sufficiently capture the semidiurnal energy-flux signal. Increasing the sampling rate and time-series duration reduces aliasing with the near-inertial frequency. These two frequencies become more difficult to distinguish at higher latitudes, as the near-inertial frequency approaches the semidiurnal frequency. According to Nash et al. (2005), the minimum time-series duration needed to clearly distinguish between semidiurnal and near-inertial frequency waves is $T = 2\pi/(M_2 - f)$. For

Mendocino Escarpment, which is approximately 20° further north, $T = 1.4$ days. There are six profiles over 12.8 hours taken at Station 8, nearest the surface reflection, and seven profiles over 14.5 hours at Station 3, after the surface reflection, implying that aliasing may be contributing some error.

4.2.9 Momentum-Flux

The time-mean momentum-fluxes ($\langle\widetilde{u}^2\rangle_t, \langle\widetilde{u}\widetilde{v}\rangle_t, \langle\widetilde{u}\widetilde{w}\rangle_t, \langle\widetilde{v}^2\rangle_t, \langle\widetilde{v}\widetilde{w}\rangle_t, \langle\widetilde{w}^2\rangle_t$) take the form $\langle\widetilde{v}\widetilde{w}\rangle_t = 0.5(v_S w_S + v_C w_C)$. Assuming that the internal-tide beam has minimal x-dependence, the focus is on time-mean momentum-fluxes,$\langle\widetilde{v}^2\rangle_t$ and $\langle\widetilde{v}\widetilde{w}\rangle_t$, which are relevant to wave-mean interaction in (3.39). In Figure 4.10, $\langle\widetilde{v}^2\rangle_t$ is enhanced along the northward, upward beam, intensified near the surface reflection and diminished thereafter. Enhanced areas near the bottom are consistent with locations of near-critical topography. Figure 4.11 gives a similar account for $\langle\widetilde{v}\widetilde{w}\rangle_t$. The sign along the upward, northward beam is still positive at Station 8, which suggests that the surface reflection occurs north of this latitude or loss during reflection and superposition. Negligible values near the surface imply cancellation due to partial reflection (superposition of incident and reflected ray paths), but near-surface data is most prone to error. Along the reflected ray path at Station 3, the momentum-flux has changed sign which supports its association with the reflected beam. Continuing along this path, another sign change is evident; there are possible explanations including potential beam generation to the north at approximately 41° 15′ N and off-transect variability.

Finally, the remaining momentum-fluxes, $\langle\widetilde{u}\widetilde{v}\rangle_t$ and $\langle\widetilde{u}\widetilde{w}\rangle_t$ are examined. For $\langle\widetilde{u}\widetilde{v}\rangle_t$ (Figure 4.12), there does not appear to be a correlation with the ray path for a beam emanating north from the ridge, although there is a peak

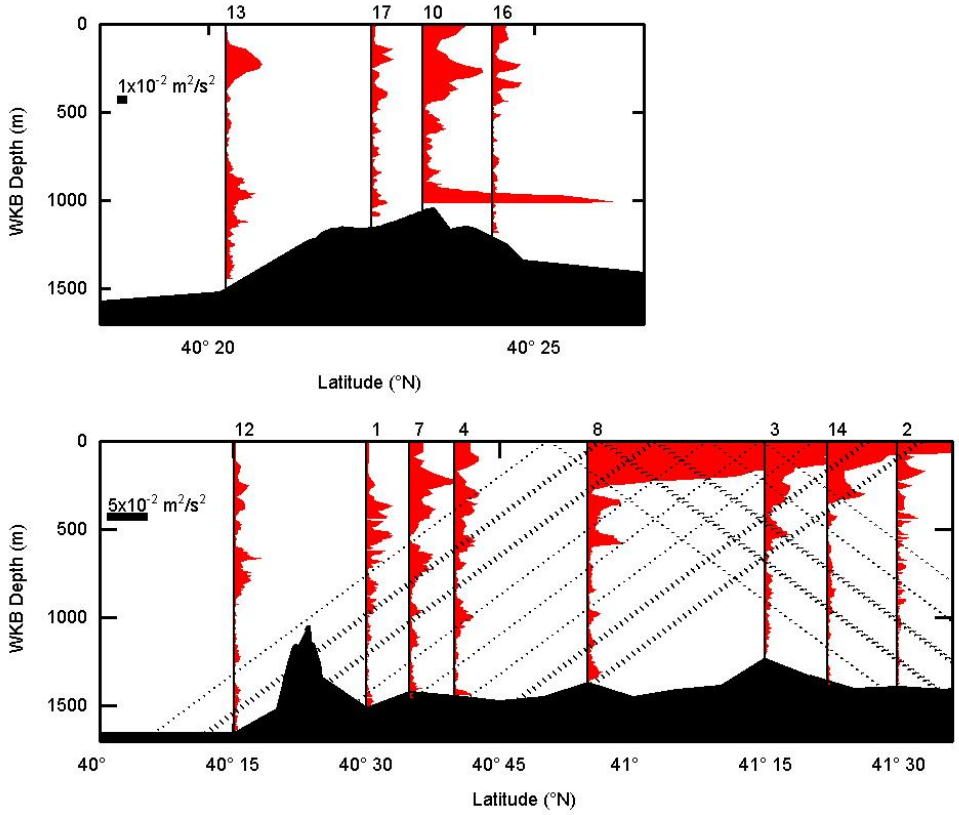

Figure 4.10: WKB-scaled time-mean momentum-fluxes, $\langle \widetilde{v}^2 \rangle_t$, for stations along the main transect where positive fluxes are red, negative are blue. Ray paths are drawn to show energy propagation of the semidiurnal wave (not shown in upper panel since scaling causes them to appear horizontal). Dotted-lines represent incident and reflected ray paths; thicker dots indicate ray paths converging on Station 3.

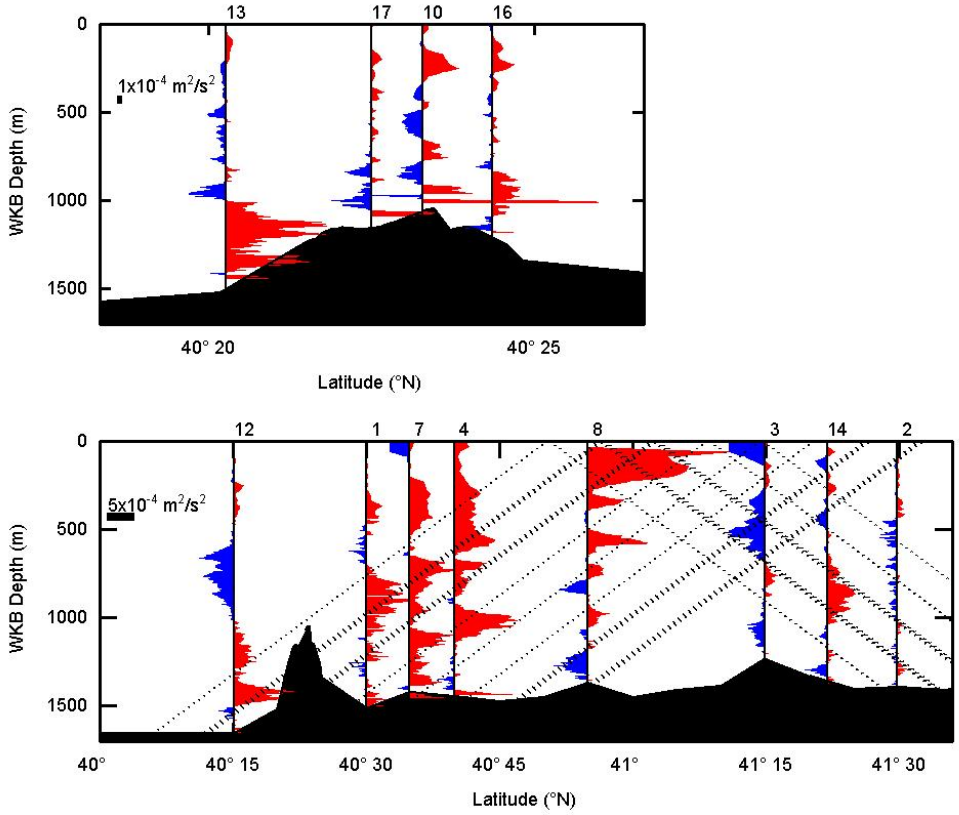

Figure 4.11: WKB-scaled time-mean momentum-fluxes, $\langle \widetilde{v}\widetilde{w} \rangle_t$, for stations along the main transect where positive fluxes are red, negative are blue. Ray paths are drawn to show energy propagation of the semidiurnal wave (not shown in upper panel since scaling causes them to appear horizontal). Dotted-lines represent incident and reflected ray paths; thicker dots indicate ray paths converging on Station 3.

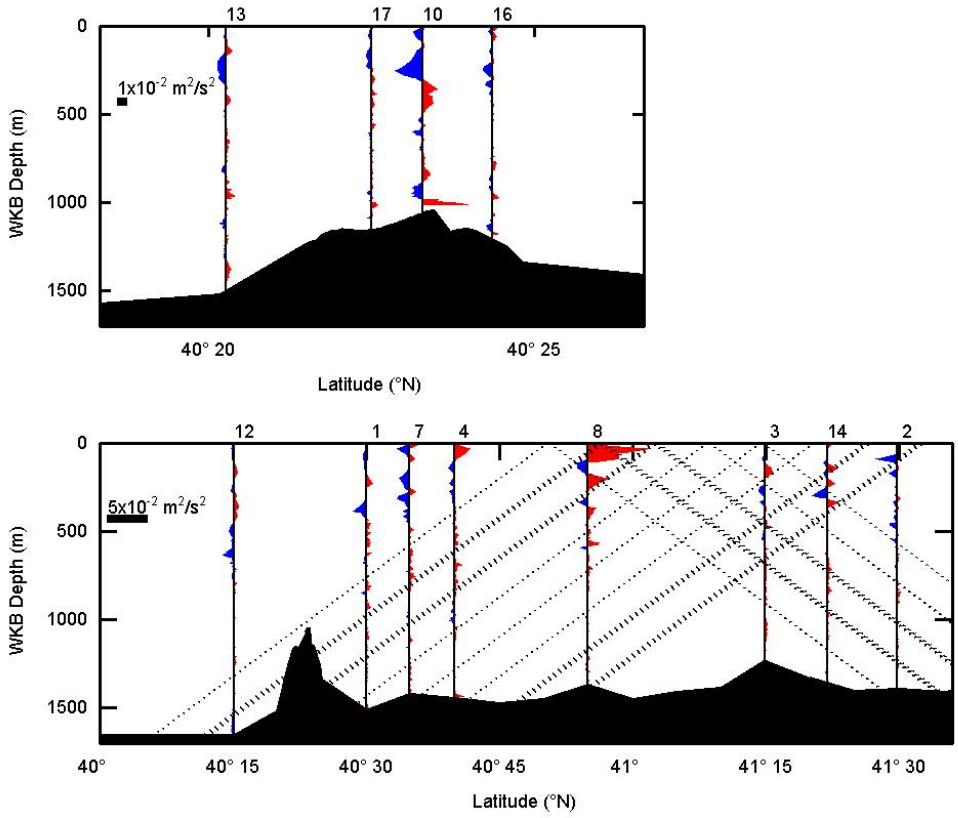

Figure 4.12: WKB-scaled time-mean momentum-fluxes, $\langle \widetilde{u}\widetilde{v} \rangle_t$, for stations along the main transect where positive fluxes are red, negative are blue. Ray paths are drawn to show energy propagation of the semidiurnal wave (not shown in upper panel since scaling causes them to appear horizontal). Dotted-lines represent incident and reflected ray paths; thicker dots indicate ray paths converging on Station 3.

near the surface reflection. Values are about an order of magnitude smaller than $\langle \widetilde{v}^2 \rangle_t$. These smaller values are consistent with zonal or meridional propagation, but not diagonal. Enhancements can also be seen near ray-paths to the south. In general, these smaller values support a weaker dependence on x. Values of $\langle \widetilde{u}\widetilde{w} \rangle_t$ (Figure 4.13) are significantly smaller than $\langle \widetilde{v}\widetilde{w} \rangle_t$, with the exception of Stations 7, 4 and 8 along the beam path.

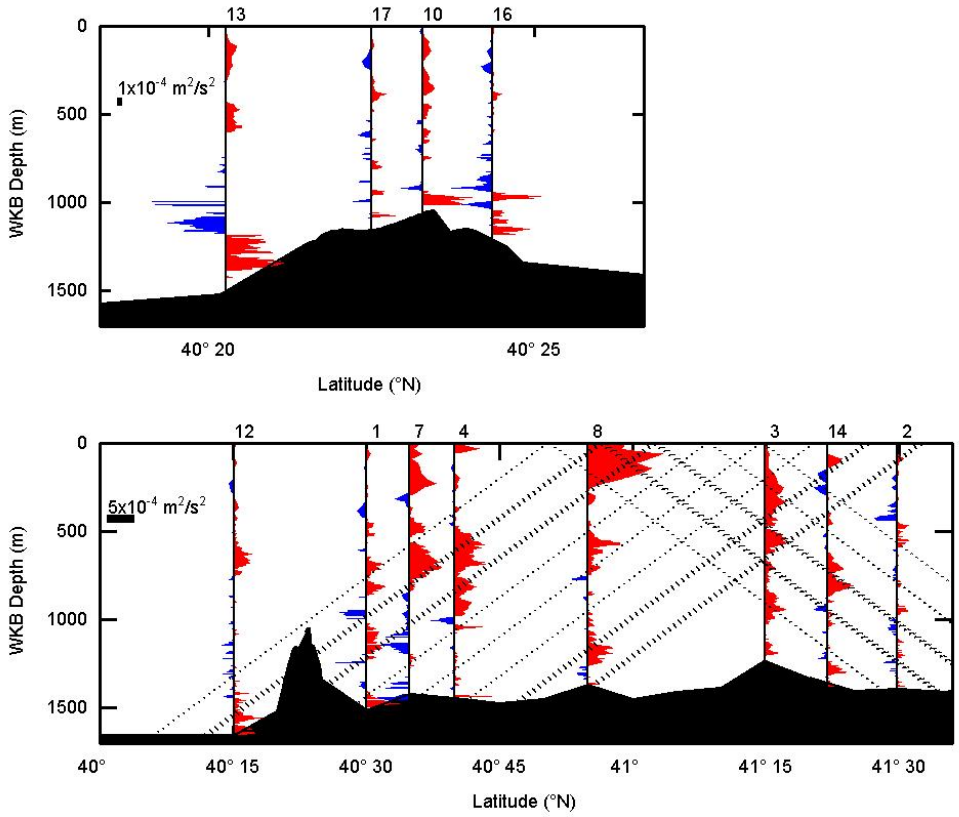

Figure 4.13: WKB-scaled time-mean momentum-fluxes, $\langle \widetilde{u}\widetilde{w} \rangle_t$, for stations along the main transect where positive fluxes are red, negative are blue. Ray paths are drawn to show energy propagation of the semidiurnal wave. Dotted-lines represent incident and reflected ray paths; thicker dots indicate ray paths converging on Station 3.

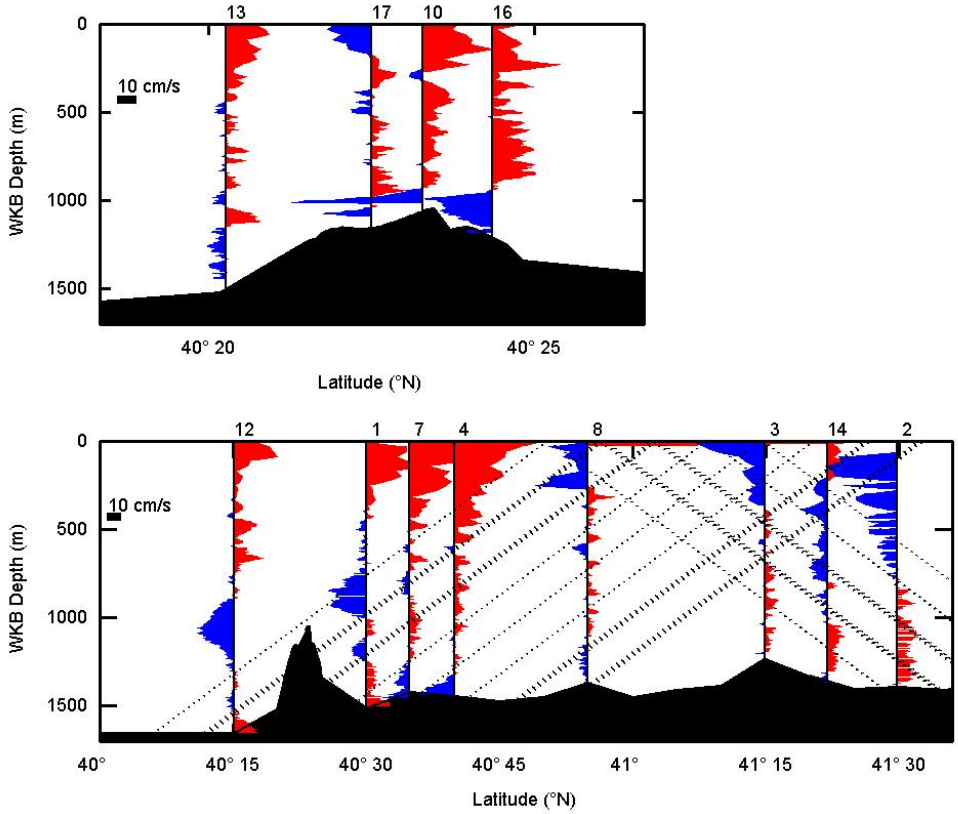

Figure 4.14: WKB-scaled time-mean baroclinic zonal velocity, u_0, based on the least-squares fits for stations along the main transect where eastward is are red, westward are blue. Ray paths are drawn to show energy propagation of the semidiurnal wave (not shown in upper panel since scaling causes them to appear horizontal). Dotted-lines represent incident and reflected ray paths; thicker dots indicate ray paths converging on Station 3.

4.2.10 Mean Flow

Baroclinic time-mean velocities, u_0 and v_0, are evaluated from the least-squares fits. These magnitudes may be compromised by inertial internal waves since this effect cannot be properly extracted with these time series. Based on the fits, there is no obvious correlation between the WKB-scaled time-mean velocities and the beam (Figures 4.14 and 4.15). Wind- or eddy-driven flows may also complicate the dynamics, especially near the surface.

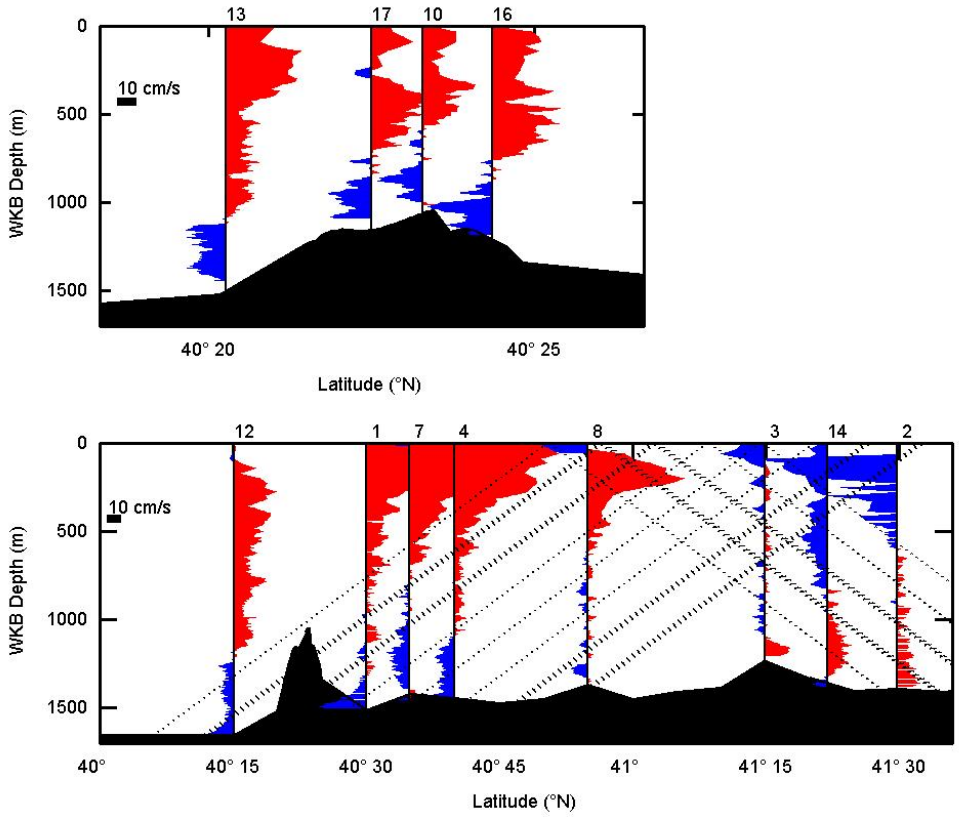

Figure 4.15: WKB-scaled time-mean baroclinic meridional velocity, v_0, based on the least-squares fits for stations along the main transect where eastward is are red, westward are blue. Ray paths are drawn to show energy propagation of the semidiurnal wave (not shown in upper panel since scaling causes them to appear horizontal). Dotted-lines represent incident and reflected ray paths; thicker dots indicate ray paths converging on Station 3.

4.2.11 Isopycnals

Time-mean isopycnals are examined meridionally and zonally in order to determine whether there are horizontal density gradients to assess variability in the region. The contour plot in Figure 4.16a shows results along the main transect. Stations are concentrated near the ridge, giving better resolution in that region and possibly a misleading impression of more meridional structure there. A steady-state anomaly in the isopycnals is located over the ridge. Away from the ridge, the isopycnals appear to become more level (but resolution is inadequate).

Figure 4.16b approximates the zonal isopycnals. Below 200 m, the density gradient is positive. Above 200 m, the isopycnals are level. It is difficult to know whether the gradient is purely zonal, since the stations are not at the exact same latitude and this region has large meridional gradients.

4.3 Interpretation

Interpreting the energy-fluxes, momentum-fluxes and mean flows with absolute certainty is challenging given the vast amount of spatial information missing. This investigation targets contributions to the near-surface peak at Station 8 and to the portion of Station 3 along the surface-reflected beam's path.

Consider first the near-surface peak at Station 8 in Figures 4.7, 4.10, 4.11 and 4.13. Three potential situations are considered for the beam in this region: (i) upward-propagating before reflection, (ii) superposition with its own reflection, (iii) superposition with another northward, upward propagating beam originating along the ridge. The credibility of each is described in

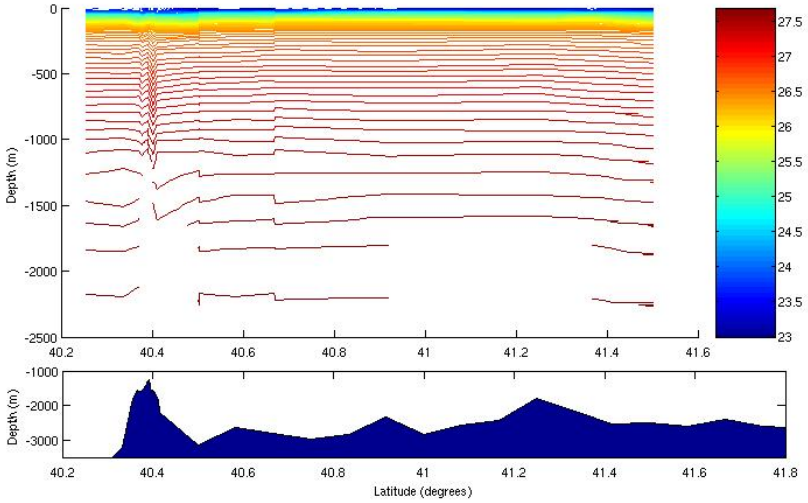

(a) across flank

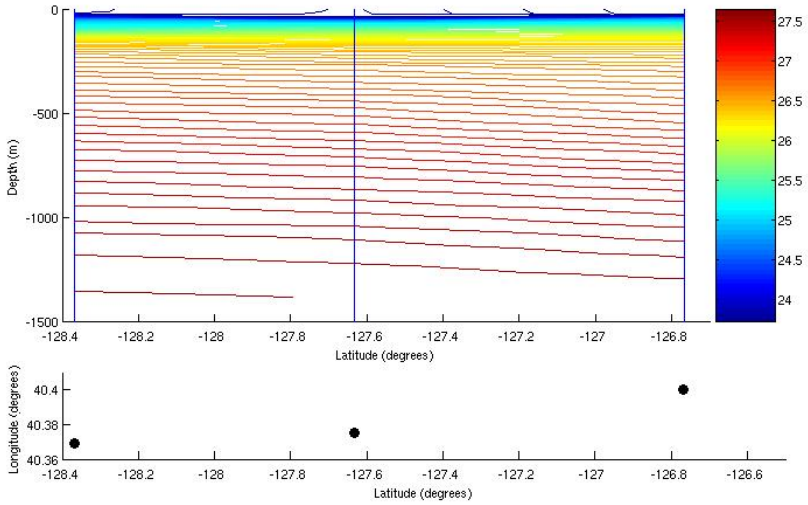

(b) along flank

Figure 4.16: Potential density contours a) across flank and b) along flank at at Mendocino Escarpment, estimated from profile data. The bathymetry is plotted beneath for comparison. The vertical lines in b) denote the longitudinal location of the stations. The lower panel gives the coordinates of the stations.

turn. First, while energy- and momentum-fluxes along the ray path emanating from the ridge (prior to Station 8) indicate an upward-propagating beam, their magnitudes are smaller than those observed near-surface at Station 8. The signs of energy- and momentum-fluxes suggest upward propagation up to and including Station 8. Modulation due to spring-neap tides may be occurring, with spring tides occurring shortly after full or new moon phases. It would be interesting to have a longer time-series of the internal tide at Mendocino Escarpment to see if there is time dependence associated with the spring-neap cycle, such as that found by Ledwell et al (2000) at the Mid-Atlantic Ridge. Although modulation is unknown without this data, large velocities at Station 8 are not entirely surprising since these profiles occurred 3 days after the new moon. Second, superposition with its own reflection does account for the intensification of $\langle\widetilde{v}^2\rangle_t$, but $\langle\widetilde{v}\widetilde{w}\rangle_t$ should be much smaller due to cancellation in vertical velocities. The peak for $\langle\widetilde{v}\widetilde{w}\rangle_t$ is slightly deeper than for $\langle\widetilde{v}^2\rangle_t$, suggesting superposition may be occurring very close to the surface at the leading edge of the superposition region. Energy-fluxes (Figure 4.7) do not flatten enough to support complete superposition, but the shallowest depths indicate some cancellation. Third, superposition with another off-transect north- and upward-propagating beam offset zonally (generated further along the ridge) is a possibility. This could account for intensified momentum-fluxes ($\langle\widetilde{v}^2\rangle_t$, $\langle\widetilde{v}\widetilde{w}\rangle_t$). Zonal energy-fluxes in Figure 4.8 do not support this hypothesis though Althaus et al. (2003) show large eastward zonal fluxes. While each scenario is speculative, taken together, it appears that this profile is at the south edge of the superposition region, with most of the beam still upward-propagating. Without more information, the third scenario cannot be properly verified.

Next, contributions to $\langle\widetilde{v}^2\rangle_t$ and $\langle\widetilde{v}\widetilde{w}\rangle_t$ momentum-fluxes of Station 3 in the beam pathway are assessed. Either these fluxes can be explained by (i) the main internal tide beam, (ii) other along-transect internal tide beams, (iii) off-transect internal tide beams, or (iv) fortnightly temporal variability modulating the internal tide amplitudes. First, we determine whether the main internal tide beam is responsible. Momentum-fluxes $\langle\widetilde{v}^2\rangle_t$ and $\langle\widetilde{v}\widetilde{w}\rangle_t$, and meridional and vertical energy-fluxes, at this station are in agreement with expectations of an internal tide beam reflected off the surface. Since the energy-flux calculated by Althaus et al. (2003) is in a conflicting direction, we must proceed cautiously. To the north, the magnitude of $\langle\widetilde{v}^2\rangle_t$ and the energy-fluxes diminish, and $\langle\widetilde{v}\widetilde{w}\rangle_t$ implies an opposing propagation direction. Internal tide dissipation in the intervening region between Stations 3 and 14 could explain the changes in magnitude and sign, but there is no supporting evidence. Inferred dissipation rates by Althaus et al. are negligible in this region. We conclude that the main internal tide beam is not a major contributor to fluxes after the surface reflection. Second, along-transect possibilities are evaluated. In $\langle\widetilde{v}^2\rangle_t$, there is a small peak at the bottom of Station 8. It appears that this could propagate upward and northward, intersecting the beam path at Station 3. However, since $\langle\widetilde{v}\widetilde{w}\rangle_t$ is negative near the bottom of Station 9, upward and northward momentum-flux is not possible. This fact is emphasized by the meridional and vertical energy-fluxes which are northward and downward there. Similarly, stations to the north do not indicate any sources for the momentum-fluxes since inferred directions of propagation are not compatible. Third, off-transect possibilities are considered. Zonal energy-flux in Figure 4.8 does indicate that another beam could be intersecting from the east. Fourth, the amplitude

of the internal tide is modulated by the spring-neap tides. Unfortunately, this time-series is insufficient to isolate this effect. For now, it is assumed that the semidiurnal internal wave generated at Mendocino Escarpment is a wave train, rather than a group, with ray-like propagation, such that the superposition region does not change over time. Overall, with the available information, it seems most likely that an off-transect beam is responsible for the fluxes of Station 3 in the beam pathway. Assuming that this is true, the internal tide beam generated at the ridge is significantly reduced after the surface reflection. This along-beam gradient implies that internal wave momentum-flux divergences are non-zero and a mean flow could be induced.

Decreases in energy-flux after the reflection are associated with large inferred dissipation rates (Althaus et al., 2003). The energy- and momentum-fluxes reveal that the internal tide beam is reduced after the first surface reflection. These reductions and dissipation motivate further theoretical analysis of the momentum-flux divergences at the surface reflection, where it is assumed that energy is dissipated through wave breaking due to superposition of incident and reflected rays.

Chapter 5

Case Studies

Three case studies are used to examine momentum-flux divergence forcing and the time-mean zonal velocity which would result from (3.39), each one progressively building our understanding of the situation at Mendocino Escarpment. The cases are an upward-propagating internal tide beam (i) with a dissipating patch (Figures 5.3 and 5.4), (ii) reflecting off the surface without dissipation (Figures 5.5 to 5.8) and (iii) reflecting off the surface with dissipation (Figures 5.5, 5.9 and 5.10). Since changes in mean circulation induced by dissipative waves have been linked to time-mean tracer transport, we briefly examine its role in (i) to see if the same result holds, in (ii) to determine whether superposition introduces another transport mechanism, and in (iii) to assess the combined result.

This analysis makes four key assumptions:

1. There is no x-dependence (i.e., $\frac{\partial}{\partial x} = 0$ so $k = 0$).

2. The propagating wave has a beam-like structure, so that the wave field is limited to a long narrow region where the baroclinic energy is concentrated.

3. In the dissipating cases (I and III), dissipation occurs uniformly along the ray path.

4. There is constant stratification, so that the buoyancy frequency N and the vertical wavenumber m do not depend on z.

The first assumption is motivated by an idealized version of Mendocino Escarpment with a meridional barotropic flow v_{bt} over meridional topography $h(y)$ as was implied by the proposed force balance. Consequently, all internal-wave velocities satisfy the phase relations (3.29) and (3.30) for $k = 0$.

The second assumption is also motivated by Mendocino Escarpment. As indicated earlier, the energy of this internal wave beam propagates upward with slope $s = -\frac{l}{m} = \sqrt{\frac{(\omega^2-f^2)}{(N^2-\omega^2)}}$ with vertical wavenumber m negative (downward phase and upward energy propagation) and meridional wavenumber l positive. Let the along-beam velocity v^* be represented by

$$v^* = Re[H(\eta)\exp(-i\omega t)] \tag{5.1}$$

where η is parallel to phase and normal to energy propagation. We choose a beam-like form for $H(\eta)$ which only allows unidirectional propagation indicated by the limits of integration, and which is dominated by low wavenumbers in wave space (Sherman and Pinkel, 1991). By letting

$$H(\eta) = \kappa \int_0^\infty \exp(-bl^*)\exp(il^*\eta)dl^* \tag{5.2}$$

$$= \frac{\kappa(b+i\eta)}{b^2+\eta^2} \tag{5.3}$$

for $b > 0$ where l^* is the cross-beam wavenumber in the η-direction, these basic requirements are satisfied. The parameters κ and b control the amplitude

and beam width. Consequently, phase and amplitude are given by

$$\phi(\eta) = \arctan(\eta/b) \tag{5.4}$$

$$F(\eta) = \frac{\kappa}{\sqrt{b^2+\eta^2}}. \tag{5.5}$$

Near $\eta = 0$, phase tends to that of a plane wave and peak amplitude κ/b. Substituting back into (5.1), the along-beam velocity simplifies to

$$v^* = Re\{\frac{\kappa}{\sqrt{b^2+\eta^2}} \exp[i(arctan(\eta/b) - \omega t)]\}. \tag{5.6}$$

Corresponding cross-beam amplitudes for three possible parameter combinations are shown in Figure 5.1 ($\kappa = 10$ m^2/s). These three instances illustrate the interdependency between beam thickness and peak amplitude. Namely, as the beam becomes narrower, the amplitude increases. Phase propagation in the η-direction is evident in Figure 5.2 which shows the along-beam velocity at discrete times for one day.

The third simplifying assumption is utilized even though it is not physically realistic as turbulent and mixing processes are known to be patchy and the underlying processes are not explicitly represented. However, Scinocca and McFarlane (2000) demonstrated that there is no advantage to non-uniform deposition of momentum between the surface and first wave-breaking height, even though deposition of momentum into the mean flow is most likely concentrated at the breaking level. For comparison, a parameterization used in modelling wave-mean interactions pertaining to the Madden-Julian oscillator in the tropical atmosphere scales the momentum dissipation linearly with the induced mean flow using observational evidence to get the rate (Biello

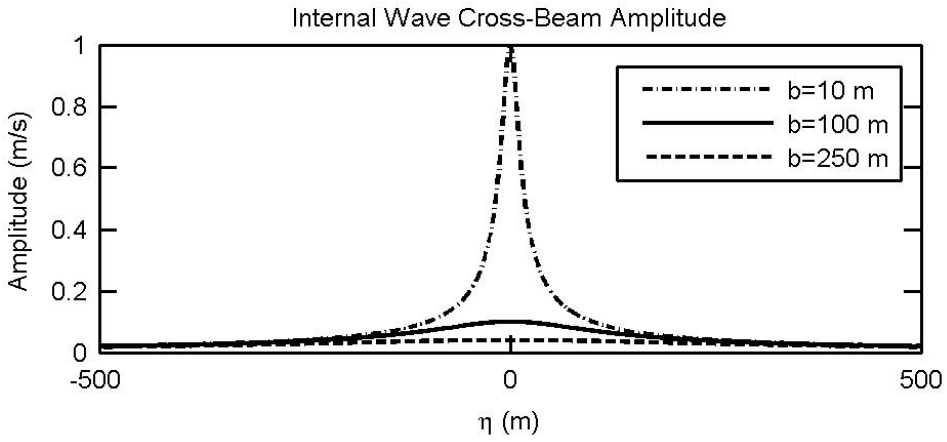

Figure 5.1: The cross-beam amplitude for an internal wave beam given by (5.6) where amplitude and beam thickness parameters are $\kappa = 10$ m^2/s and $b = 10, 100, 250$ m.

and Majda, 2005). In their case, damping is due to cloud physics which are difficult to model (Biello, 2008, personal communication).

The fourth assumption of constant buoyancy frequency ignores stratification changes with depth. Moreover, it assumes that there is no lateral variability in the stratification associated with localized turbulent mixing associated with the internal wave beam. This is reasonable as the timescale for restratification through lateral processes is on the order of a day while that associated with turbulent mixing is orders of magnitude longer. In the mixed layer, for instance, surface forcings or mesoscale flow fields induce gravitational slumping which begins the restratification process (Tandon and Garrett, 1995), after which submesoscale baroclinic instabilities are responsible for the bulk of the mixed-layer restratification (Hosegood et al., 2006; Boccaletti et al., 2007). Given that the time-mean eddy diffusivity near the surface reflection at Mendocino Escarpment is O(10^{-4}) m^2/s (Althaus et al., 2003), more than 1000 days would be required to fully mix the upper 100

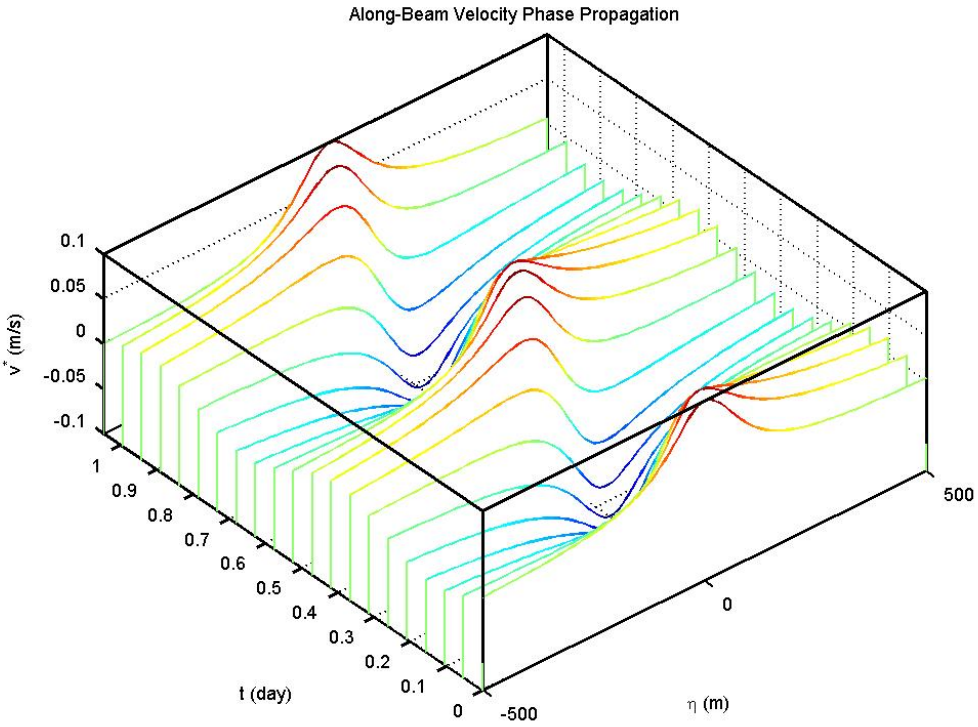

Figure 5.2: Along-beam velocity phase propagation for an internal wave beam given by (5.6) over one day where amplitude and beam thickness parameters are $\kappa = 10$ m^2/s and $b = 100$ m.

Table 5.1: Parameter values for internal tide beam (5.2-5.6)

Parameter	Definition	Value
f	Coriolis frequency	0.942×10^{-4} rad/sec
$\omega = M_2$	semidiurnal frequency	1.4075×10^{-4} rad/sec
N	buoyancy frequency	0.0052 rad/sec
s	ray slope	2.0119×10^{-2}
κ	amplitude parameter	10 m^2/s
b	amplitude, beam thickness parameter	100 m

m since $\frac{10^4 \mathrm{m}^2}{10^{-4}\mathrm{m}^2\mathrm{s}^{-1}} = 10^8$ s. If the restratification time-scale on the order of a day, the stratification would remain essentially constant. Laboratory experiments (McPhee-Shaw and Kunze, 2002) and observations (Kunze et al., 2002) of elevated boundary mixing on slopes find that stratification is maintained during turbulent mixing, likely through lateral exchange processes. Thus, constant stratification will be employed on the premise that any perturbations are small and quickly removed.

The parameters in Table 5.1 are relevant to M_2 internal tides at Mendocino Escarpment. The buoyancy frequency N is identical to that used in the WKB-scaling (Chap. 4). Amplitude and beam thickness parameters were chosen to correspond with those at Mendocino Escarpment (Figure 5.1). The resulting values agree with typical values in the Mendocino Escarpment data (e.g., Figure 4.4). Given these assumptions, we can proceed in quantifying momentum-fluxes and induced mean zonal flow for each case. Throughout, we focus on time-mean momentum-fluxes $\langle \widetilde{v}^2 \rangle_t$ and $\langle \widetilde{v}\widetilde{w} \rangle_t$ relevant to the 2-D wave-mean interaction described by (3.39).

5.1 Case I: An Upward-Propagating Internal Wave Beam with Dissipation

The setup for an upward-propagating internal wave beam with dissipation is shown in Figure 5.3. The upward-propagating wave is assumed to dissipate by a constant ratio over the dissipation region (Region 2), halving the initial momentum-flux (Region 1). The yz-axes denote meridional and vertical directions, while the primed axes denote a rotation such that the η-axis is parallel to wave phase propagation paths and y' parallel to energy propagation. Mathematically,

$$\begin{aligned}(y', \eta) &= (y\cos\theta + z\sin\theta, y\sin\theta - z\cos\theta) \\ &= \left(\frac{y+sz}{\sqrt{s^2+1}}, \frac{sy-z}{\sqrt{s^2+1}}\right). \end{aligned} \tag{5.7}$$

the direction of η corresponds to an upward-propagating internal wave with downward phase propagation.

In Region 1, the geometry is such that the meridional internal wave velocity (5.6) is

$$\widetilde{v_1} = \frac{1}{\sqrt{s^2+1}} Re\left\{\frac{\kappa}{\sqrt{b^2+\eta^2}}\exp[i(arctan(\eta/b) - \omega t)]\right\} \tag{5.8}$$

$$= \frac{\kappa}{\sqrt{b^2+\eta^2}}\frac{1}{\sqrt{s^2+1}}\cos[arctan(\eta/b) - \omega t] \tag{5.9}$$

$$= \frac{\kappa}{b^2+\eta^2}\frac{1}{\sqrt{s^2+1}}[b\cos(\omega t) + \eta\sin(\omega t)] \tag{5.10}$$

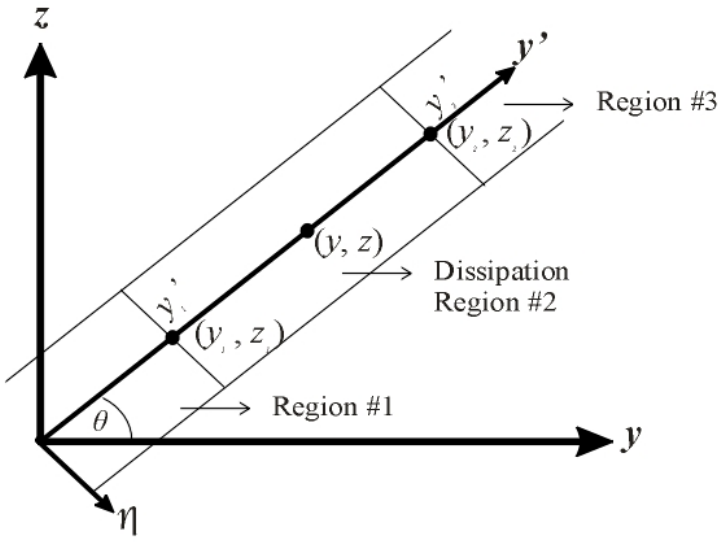

Figure 5.3: The set-up for an upward-propagating internal wave with dissipation (a) shows three regions corresponding to before (1), during (2), and after (3) dissipation. Lines of constant phase are parallel to y'.

by the identity $\cos(A-B) = \cos A \cos B + \sin A \sin B$. Similarly, the vertical internal wave velocity is

$$\widetilde{w_1} = \frac{s\kappa}{b^2+\eta^2}\frac{1}{\sqrt{s^2+1}}[b\cos(\omega t) + \eta \sin(\omega t)]. \tag{5.11}$$

Finally, zonal internal wave velocity, as obtained from (3.29), is

$$\widetilde{u_1} = \frac{f}{\omega}\frac{\kappa}{b^2+\eta^2}\frac{1}{\sqrt{s^2+1}}[-b\sin(\omega t) + \eta \cos(\omega t)]. \tag{5.12}$$

These velocities satisfy the linearized perturbation equations (3.11) - (3.14) such that (3.29) and (3.30) hold.

From these velocities, the time-mean momentum-fluxes are

$$\langle \widetilde{v_1}^2 \rangle_t = \frac{1}{s^2+1} \frac{\kappa^2}{2(b^2+\eta^2)} \tag{5.13}$$

$$\langle \widetilde{v_1}\widetilde{w_1} \rangle_t = s\langle \widetilde{v_1}^2 \rangle_t \tag{5.14}$$

where averaging is over one wave period. Thus, forcing for the v-momentum equation (3.39) is

$$\begin{aligned} \frac{\partial}{\partial y}\langle \widetilde{v_1}^2 \rangle_t + \frac{\partial}{\partial z}\langle \widetilde{v_1}\widetilde{w_1} \rangle_t &= \frac{\kappa^2}{2(s^2+1)} \left[\frac{-2\eta}{b^2+\eta^2}\frac{\partial \eta}{\partial y} - \frac{2s\eta}{b^2+\eta^2}\frac{\partial \eta}{\partial z} \right] \\ &= 0 \end{aligned} \tag{5.15}$$

since $\frac{\partial \eta}{\partial y} = -s\frac{\partial \eta}{\partial z} = \frac{s}{\sqrt{s^2+1}}$. As expected, there is no net forcing due to the momentum-flux divergences in Region 1.

In Region 3, after dissipation has occurred, the internal wave momentum-fluxes are halved compared to Region 1. Since this reduction is represented by a scalar coefficient, forcing for the v-momentum equation remains zero.

In the dissipation region (Region 2), the internal wave velocities are

$$(\widetilde{u_2}, \widetilde{v_2}, \widetilde{w_2}) = G(y')(\widetilde{u_1}, \widetilde{v_1}, \widetilde{w_1}) \tag{5.16}$$

where $G(y') = \left[1 + (\frac{1}{\sqrt{2}} - 1)\frac{y'-y_1'}{y_2'-y_1'}\right]$ to account for linear decay of the velocity along the ray. By substitution, the linearly decaying dissipation function becomes

$$G[y'(y,z)] = 1 + \left(\frac{1}{\sqrt{2}} - 1\right) \frac{y + sz - y_1 - sz_1}{y_2 + sz_2 - y_1 - sz_1}. \tag{5.17}$$

Under certain conditions, these decaying velocities still satisfy the linearized perturbation equations (3.11) - (3.14) to first order, such that relations (3.29) and (3.30) hold. For (3.11), $\frac{\partial}{\partial x} = 0$ yields (3.29). Since $\frac{\partial v^*}{\partial y'} \neq 0$, the continuity equation $\frac{\partial \widetilde{v}}{\partial y} + \frac{\partial \widetilde{w}}{\partial z} = 0$ does not hold. This relation implies that there must be convergent or divergent flows in the η- or x-directions. The continuity equation is, however, satisfied to first order when the dissipation length $y_2 - y_1$ is sufficiently large compared to the horizontal width of the beam. At second order, dissipation and time-mean momentum-flux divergences scale together.

The time-mean momentum-fluxes are

$$\langle \widetilde{v_2}^2 \rangle_t = \frac{\kappa^2 G^2(y')}{2(s^2+1)(b^2+\eta^2)} \tag{5.18}$$

$$\langle \widetilde{v_2}\widetilde{w_2} \rangle_t = s\langle \widetilde{v_2}^2 \rangle_t. \tag{5.19}$$

After some algebra, the forcing on the mean flow is

$$\frac{\partial}{\partial y}\langle \widetilde{v_2}^2 \rangle_t + \frac{\partial}{\partial z}\langle \widetilde{v_2}\widetilde{w_2} \rangle_t = \frac{\kappa^2}{L(b^2+\eta^2)} \left(\frac{1}{\sqrt{2}} - 1 \right) \frac{1}{\sqrt{s^2+1}} G(y') \tag{5.20}$$

where $L = y_2' - y_1'$ is the along-beam dissipation length. In yz-coordinates, forcing $\frac{\partial}{\partial y}\langle \widetilde{v_2}^2 \rangle_t + \frac{\partial}{\partial z}\langle \widetilde{v_2}\widetilde{w_2} \rangle_t$ becomes

$$\frac{\kappa^2\sqrt{1+s^2}}{L[b^2(s^2+1)+(sy-z)^2]} \left[\frac{1}{\sqrt{2}} - 1 + \left(\frac{3}{2} - \frac{2}{\sqrt{2}} \right) \frac{y+sz}{y_2+sz_2} \right] \tag{5.21}$$

where y_1, z_1 have been arbitrarily set to the origin (0, 0). The result is strictly positive. This implies that dissipation induces momentum-flux divergence forcing of purely eastward flows (3.39). The same result follows for a dissipating downward-propagating internal wave beam. Westerly flows

result when the dissipating internal tide beam propagates southward.

While the forcing at any given point within the dissipating region is dependent on the total length of the dissipation region L, the total transport is independent of its length since

$$\begin{aligned}\int_{y_1}^{y_2}\int_{z_1}^{z_2}\overline{u}dydz &= \int_{y_1'}^{y_2'}\overline{u}dy' \\ &= \frac{-\kappa^2}{fL(b^2+\eta^2)}\left(\frac{1}{\sqrt{2}}-1\right)\frac{1}{\sqrt{1+s^2}}\int_{y_1'}^{y_2'}G(y')dy' \\ &= \frac{-\kappa^2}{2f(b^2+\eta^2)}\left(\frac{1}{\sqrt{2}}-1\right)^2\frac{1}{\sqrt{1+s^2}}. \qquad (5.22)\end{aligned}$$

Using Table 5.1 parameter values, forcing and zonal mean velocities are shown in Figure 5.4 for three dissipation lengths. The forcing magnitude when the dissipation is 100 m decays linearly from 3.34×10^{-5} to 2.3×10^{-5} m/s^2, inducing an eastward velocity of 0.35 to 0.25 m/s. Increasing the dissipation distance by an order of magnitude decreases the forcing and associated zonal velocity by an order of magnitude. Thus, the same amount of decay concentrated over a shorter interval influences the subinertial flow to a greater degree. These velocities are uncertain, however, since a 100 m dissipation length is too short to satisfy the continuity equation to first order.

This case demonstrates that an established freely propagating internal wave beam does not generate mean flows in the absence of dissipation. This outcome does not necessarily apply during the initial establishment of a beam (Bretherton and Garrett, 1968). As the beam dissipates, second order nonlinear effects generate mean flows.

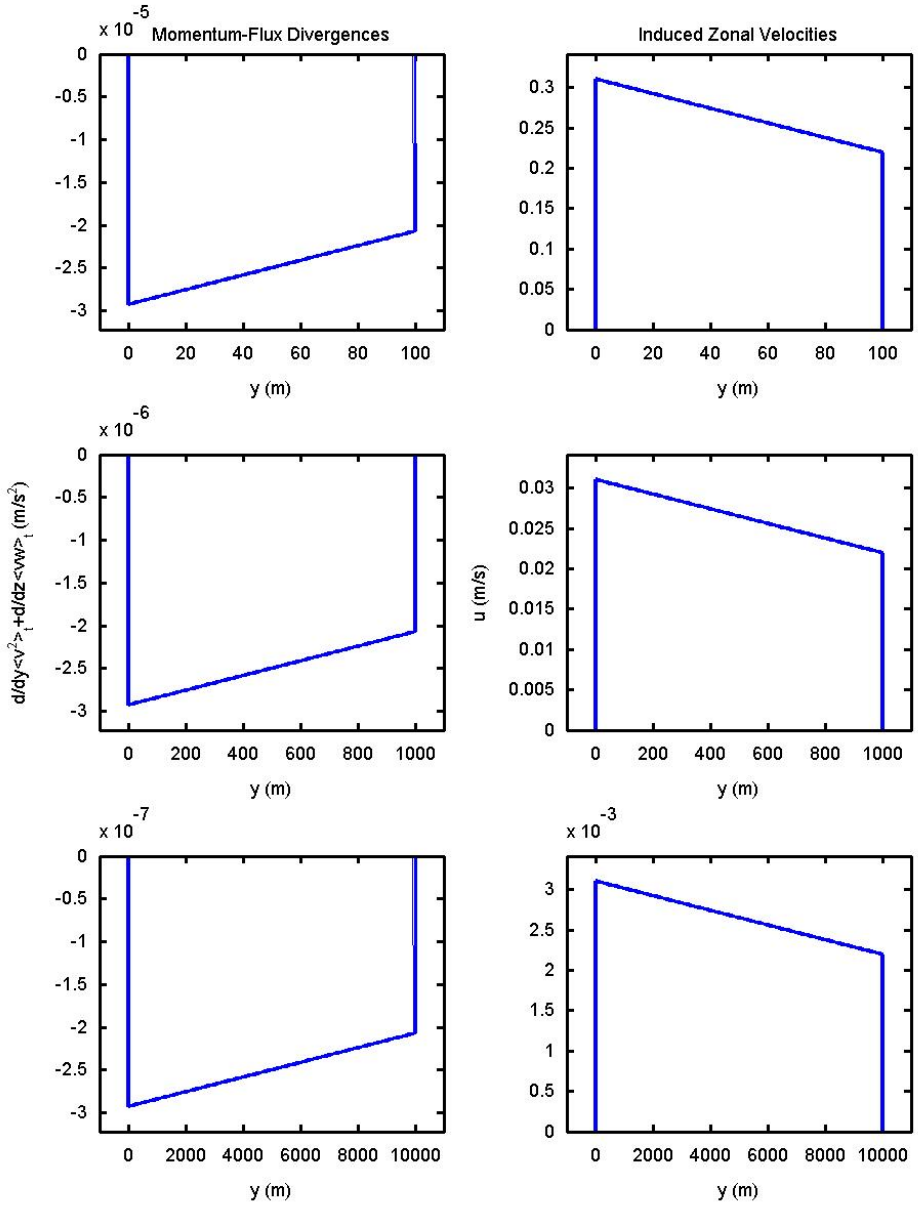

Figure 5.4: Momentum-flux divergence (at left) and associated time-mean zonal velocity $\overline{u}$ (at right) are computed for three different dissipation lengths (L=100, 1000, 10000 m).

5.2 Case II: Superposition of an Upward-Propagating Wave and its Reflection without Dissipation

The case where superposition occurs between an incident upgoing beam and a surface-reflected downgoing beam is shown in Figure 5.5. The labelling shows (i) the incident beam before entering the superposition region, (ii) the superposition region, and (iii) the reflected beam after leaving the superposition region. In this cartoon, the beam is finite in extent, but in the more realistic formulation (5.6) the beam has long tails of diminishing amplitude which expand the superposition region. Motivated by measurement methods, the vertical line at y_p (on left) represents a profile from which the vertical thickness z_f to z_0 of a beam could be obtained. The other points illustrated along the vertical profile represent two sample depths, z'_a and z'_1, from which two ray paths cross y_p. The upgoing rays are along paths $z = sy - \eta$, while downgoing rays are along paths $z = -sy + \beta$, where η and β are constants. The point at which the two sample ray paths intersect is (y_i, z_i). As a consequence of the geometry in Figure 5.5, the $\triangle y$ traveled by a ray path in the superposition region is constant (i.e., $\triangle y = y_2 - y_1 = y_b - y_a$). The along-beam amplitudes for the incident and reflected beam are shown individually in Figure 5.6. The velocity at the beam centre is 0.1 m/s for $\kappa = 10$ m^2/s and $b = 100$ m.

For the incident beam, internal wave velocities are

$$(\widetilde{u}_{up}, \widetilde{v}_{up}, \widetilde{w}_{up}) \quad = \quad (\widetilde{u}_1, \widetilde{v}_1, \widetilde{w}_1) \tag{5.23}$$

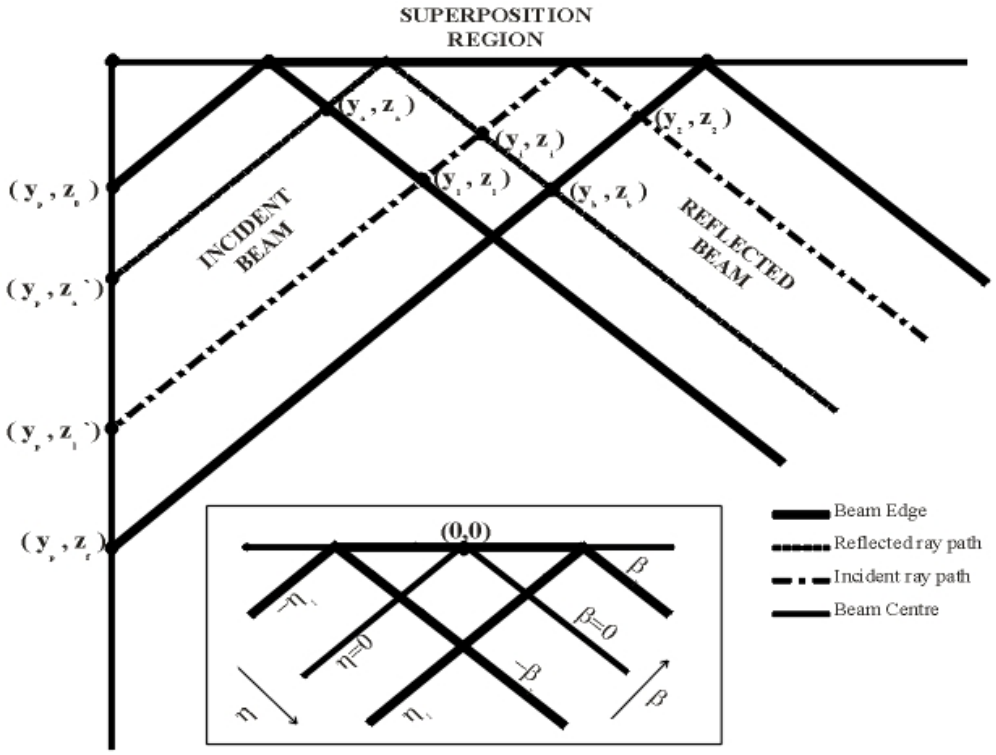

Figure 5.5: Superposition of an incident internal wave beam and its surface reflection, where thick solid lines delineate beam edges. The vertical line at y_p (left axis) represents a profile from which the vertical thickness z_f to z_0 of a beam could be obtained. Coordinates (y_i, z_i) represent a sample intersection point for ray paths (dot-dashed and dotted lines) emanating from (y_p, z_0) and (y_p, z_f). The superposition region's entry and exit coordinates for each sample ray path are also labelled. The insert highlights directions for increasing η and β, the parameters representing lines of constant phase for the internal wave beam. The origin (0, 0) is defined to be at the intersection of the $\eta = 0$ and $\beta = 0$ lines of constant phase.

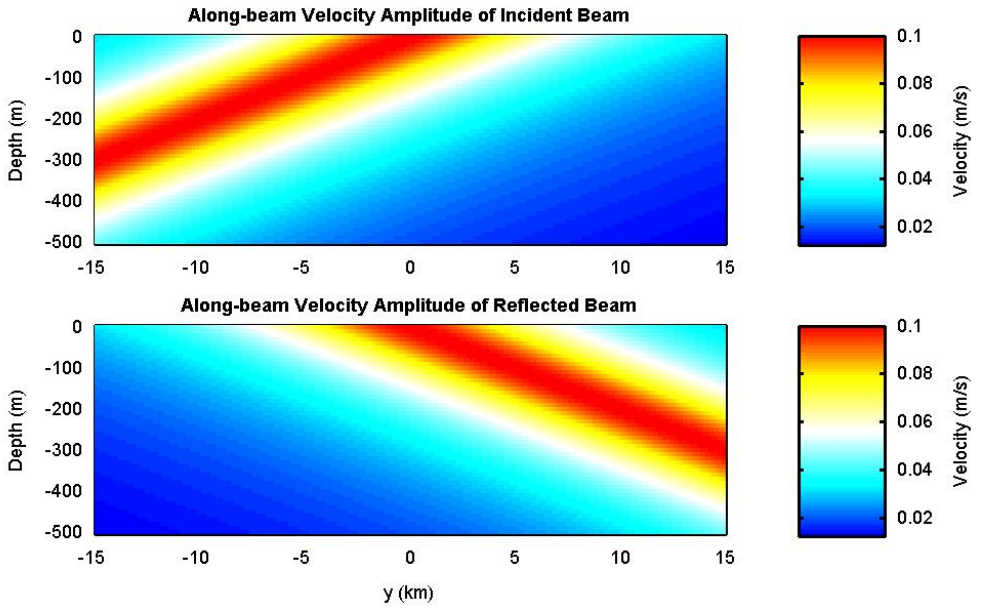

Figure 5.6: Along-beam velocity amplitudes (5.5) for the incident (upper panel) and reflected beam (lower panel) for $\kappa = 10$ m^2/s and $b = 100$ m.

from Case 1. Hence, zero forcing occurs in this region.

In the reflected beam, internal wave velocities are similarly derived from (5.6), (3.29) and (3.30) to obtain

$$\widetilde{v}_{down} = \frac{\kappa}{b^2+\beta^2}\frac{1}{\sqrt{s^2+1}}[b\cos(\omega t)+\beta\sin(\omega t)] \tag{5.24}$$

$$\widetilde{w}_{down} = \frac{-s\kappa}{b^2+\beta^2}\frac{1}{\sqrt{s^2+1}}[b\cos(\omega t)+\beta\sin(\omega t)] \tag{5.25}$$

$$\widetilde{u}_{down} = \frac{f}{\omega}\frac{\kappa}{b^2+\beta^2}\frac{1}{\sqrt{s^2+1}}[-b\sin(\omega t)+\beta\cos(\omega t)] \tag{5.26}$$

where β is the cross-beam co-ordinate (Figure 5.5). These velocities differ from the upgoing incident beam, since the vertical wavenumber m changes sign such that the relation between v and w also changes sign. Forcing due to momentum-flux divergence of the internal wave field is zero in the reflected beam as in the incident beam.

In the superposition region

$$\begin{aligned}
\widetilde{u}_{sup} &= \widetilde{u}_{up} + \widetilde{u}_{down} \\
&= \frac{f\kappa}{\omega\sqrt{s^2+1}(b^2+\eta^2)(b^2+\beta^2)} \left\{ -b\sin(\omega t)(2b^2+\beta^2+\eta^2) \right. \\
&\quad \left. + \cos(\omega t)[\eta(b^2+\beta^2)+\beta(b^2+\eta^2)] \right\} \qquad (5.27) \\
\widetilde{v}_{sup} &= \frac{\kappa}{\sqrt{s^2+1}(b^2+\eta^2)(b^2+\beta^2)} \left\{ b\cos(\omega t)(2b^2+\beta^2+\eta^2) \right. \\
&\quad \left. + \sin(\omega t)[\eta(b^2+\beta^2)+\beta(b^2+\eta^2)] \right\} \qquad (5.28) \\
\widetilde{w}_{sup} &= \frac{s\kappa}{\sqrt{s^2+1}(b^2+\eta^2)(b^2+\beta^2)} \left\{ b\cos(\omega t)(\beta^2-\eta^2) \right. \\
&\quad \left. + \sin(\omega t)[\eta(b^2+\beta^2)-\beta(b^2+\eta^2)] \right\}. \qquad (5.29)
\end{aligned}$$

At the surface ($z = 0$), $\eta = \beta$ and, hence, $\widetilde{w}_{sup} = 0$ as required.

The time-mean momentum-fluxes are

$$\begin{aligned}
\langle \widetilde{v}^2_{sup} \rangle_t &= \frac{\kappa^2(4b^2+\beta^2+\eta^2+2\eta\beta)}{2(s^2+1)(b^2+\eta^2)(b^2+\beta^2)} \qquad (5.30) \\
\langle \widetilde{v}_{sup}\widetilde{w}_{sup} \rangle_t &= \frac{s\kappa^2(\beta^2-\eta^2)}{2(s^2+1)(b^2+\eta^2)(b^2+\beta^2)}. \qquad (5.31)
\end{aligned}$$

Meridional time-mean momentum-fluxes $\langle \widetilde{v}^2_{sup} \rangle_t$ are positive-definite and additive when superimposed, while vertical time-mean momentum-fluxes $\langle \widetilde{v}_{sup}\widetilde{w}_{sup} \rangle_t$ change sign after the surface reflection and negate one another (Figure 5.7).

To derive the total forcing, individual meridional and vertical momentum-

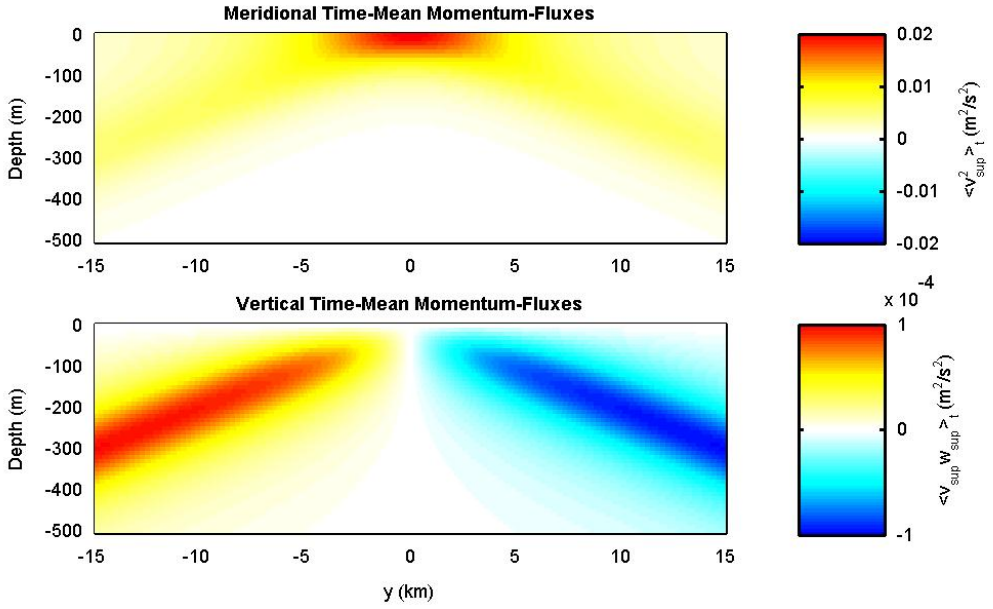

Figure 5.7: Time-mean momentum-fluxes $\langle \widetilde{v}^2_{sup} \rangle$ (upper panel) and $\langle \widetilde{v}_{sup} \widetilde{w}_{sup} \rangle$ (lower panel) for the superimposed beams (5.30)-(5.31) with $\kappa = 10\ \mathrm{m}^2/\mathrm{s}$ and $b = 100$ m.

flux divergence components are

$$\frac{\partial}{\partial y}\langle\widetilde{v}_{sup}^2\rangle_t = \frac{\kappa^2}{(s^2+1)(b^2+\eta^2)(b^2+\beta^2)}\frac{\partial\eta}{\partial y}\Bigg[2\beta+2\eta- (4b^2+\beta^2+\eta^2+2\eta\beta)\left(\frac{\eta}{b^2+\eta^2}+\frac{\beta}{b^2+\beta^2}\right)\Bigg] \quad (5.32)$$

$$\frac{\partial}{\partial z}\langle\widetilde{v}_{sup}\widetilde{w}_{sup}\rangle_t = \frac{\kappa^2}{(s^2+1)(b^2+\eta^2)(b^2+\beta^2)}\frac{\partial\eta}{\partial y}\Bigg[\beta+\eta+ (\beta^2-\eta^2)\left(\frac{\eta}{b^2+\eta^2}-\frac{\beta}{b^2+\beta^2}\right)\Bigg]. \quad (5.33)$$

The derivation incorporates the cross-beam coordinate relationships, $\frac{\partial\eta}{\partial y} = \frac{\partial\beta}{\partial y}$, $\frac{\partial\eta}{\partial z} = -\frac{\partial\beta}{\partial z}$ and $\frac{\partial\eta}{\partial z} = \frac{-1}{s}\frac{\partial\eta}{\partial y}$. The combined forcing is

$$\frac{\partial}{\partial y}\langle\widetilde{v}_{sup}^2\rangle_t + \frac{\partial}{\partial z}\langle\widetilde{v}_{sup}\widetilde{w}_{sup}\rangle_t = \frac{s\kappa^2}{(s^2+1)^{1.5}(b^2+\eta^2)(b^2+\beta^2)}\Bigg[\beta+\eta- (2b^2+2\eta\beta)\left(\frac{\eta}{b^2+\eta^2}+\frac{\beta}{b^2+\beta^2}\right)\Bigg]. \quad (5.34)$$

This forcing is somewhat surprising given Thorpe's (1999) result that no along-slope currents are generated by superposition of internal waves reflecting off a sloping bottom in the absence of dissipation. However, his analysis was limited to $\langle\widetilde{v}\widetilde{w}\rangle_t$ and lacked beam structure, a fundamental contributor to the forcing derived here.

Substituting in parameter values from Table 5.1, the momentum-flux divergence forcing and mean zonal mean velocity deduced from (3.39) are shown in Figure 5.8. Momentum-flux divergence forcing is concentrated in the upper 50 m and within 5 km of the superposition centre, with peak values of $\pm 1.3 \times 10^{-6}$ m/s^2. Peak zonal velocities are ± 0.014 m/s. The forcing and resulting flow are antisymmetric about the superposition centre, with four jets opposing one another meridionally and vertically. The weaker subsurface

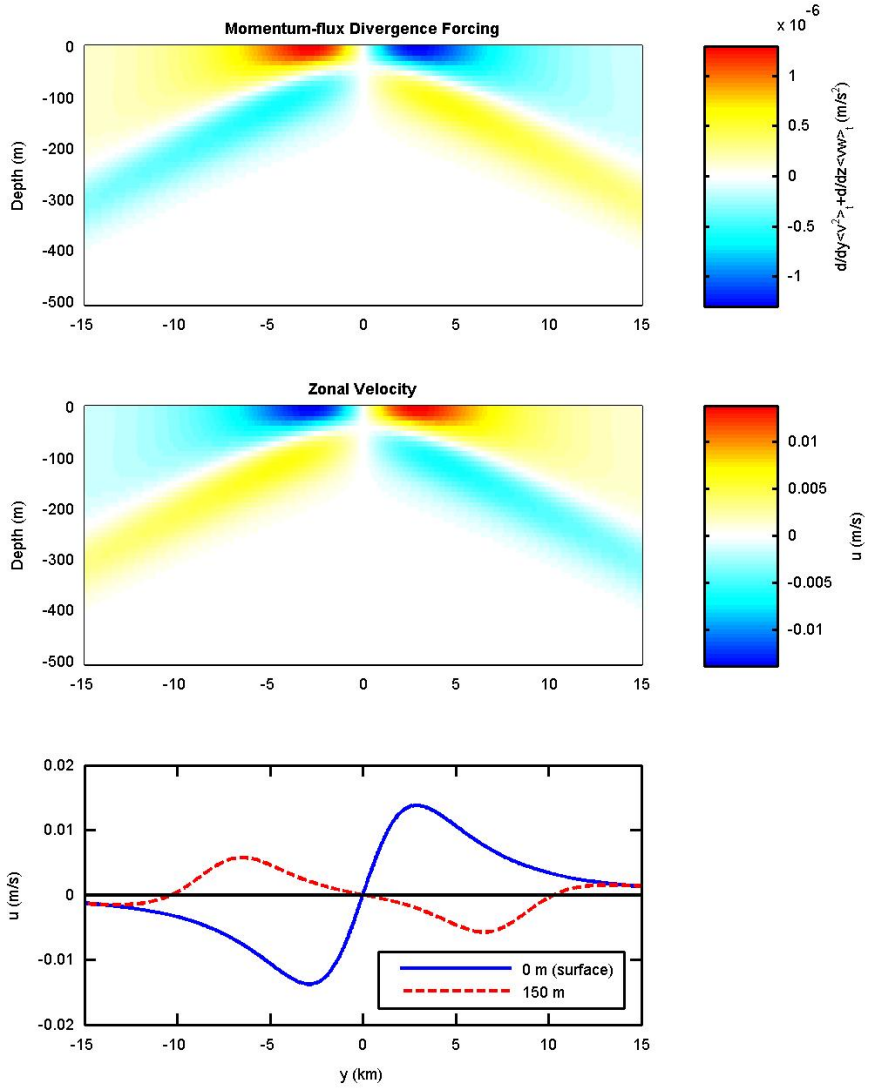

Figure 5.8: Momentum-flux divergence forcing (upper panel) and resulting zonal velocity (middle panel) caused by the superposition of an upward-propagating wave and its reflection without dissipation through the superposition region. Horizontal profiles of time-mean zonal velocity (lower panel) at the surface (0 m) and 150 m depth show opposing jets meridionally and vertically.

jets (100-200 m) have velocities a factor of 2 less than the surface jets, shown clearly by the horizontal slices in the lower panel.

The zonal jet pattern is most easily understood by viewing the internal wave time-mean momentum-fluxes in Figure 5.7. The meridional gradients in the upper panel correspond to the two surface jets, while the depth-gradients in the lower panel correspond to the two subsurface jets.

The subinertial flow induced by the momentum-flux divergences resulting from superposition at a surface reflection without dissipation has not been previously considered. The flow induced by the momentum-flux divergences may be counteracted partially by the Stokes drift. Given that the induced flow is comparable to surface velocities driven by wind and other mechanisms, this process deserves further consideration.

5.3 Case III: Superposition of an Upward-Propagating Wave and its Reflection with Dissipation

In this second case of superposition of an upward-propagating wave and its reflection, it is assumed that superposition causes dissipation. Again, we use the set-up in Figure 5.5. As in Case I, dissipation is assumed constant and to halve momentum-fluxes.

This case is relevant when an internal wave beam is generated by tidal flow as described in Section 4.2.7; nonlinear interactions are more pronounced in this circumstance as the beams are narrow and have increased shear variance (Lamb, 2004).

The incident region is unchanged. In the reflected region, the internal wave velocities are

$$\widetilde{v}_{down} = \frac{1}{\sqrt{2}}\frac{\kappa}{b^2+\beta^2}\frac{1}{\sqrt{s^2+1}}[b\cos(\omega t)+\beta\sin(\omega t)] \tag{5.35}$$

$$\widetilde{w}_{down} = \frac{1}{\sqrt{2}}\frac{-s\kappa}{b^2+\beta^2}\frac{1}{\sqrt{s^2+1}}[b\cos(\omega t)+\beta\sin(\omega t)] \tag{5.36}$$

$$\widetilde{u}_{down} = \frac{1}{\sqrt{2}}\frac{f}{\omega}\frac{\kappa}{b^2+\beta^2}\frac{1}{\sqrt{s^2+1}}[-b\sin(\omega t)+\beta\cos(\omega t)]. \tag{5.37}$$

These velocities are similar to Case II, except the magnitude has diminished. Therefore, when not superimposed, the incident and reflected beams have zero momentum-flux divergence forcing as before.

Now, we investigate the region where both superposition and dissipation occur. The superimposed internal wave velocities are

$$\begin{aligned}\widetilde{u}_{sup} &= G(y')\widetilde{u}_{up}+\sqrt{2}J(y'')\widetilde{u}_{down}\\ &= \frac{f\kappa}{\omega\sqrt{s^2+1}(b^2+\eta^2)(b^2+\beta^2)}\big\{-b\sin(\omega t)[G(b^2+\beta^2)+J(b^2+\eta^2)]\\ &\quad +\cos(\omega t)[G\eta(b^2+\beta^2)+J\beta(b^2+\eta^2)]\big\}\end{aligned} \tag{5.38}$$

$$\begin{aligned}\widetilde{v}_{sup} &= \frac{\kappa}{\sqrt{s^2+1}(b^2+\eta^2)(b^2+\beta^2)}\big\{b\cos(\omega t)[G(b^2+\beta^2)+J(b^2+\eta^2)]\\ &\quad +\sin(\omega t)[G\eta(b^2+\beta^2)+J\beta(b^2+\eta^2)]\big\}\end{aligned} \tag{5.39}$$

$$\begin{aligned}\widetilde{w}_{sup} &= \frac{s\kappa}{\sqrt{s^2+1}(b^2+\eta^2)(b^2+\beta^2)}\big\{b\cos(\omega t)[G(b^2+\beta^2)-J(b^2+\eta^2)]\\ &\quad +\sin(\omega t)[G\eta(b^2+\beta^2)-J\beta(b^2+\eta^2)]\big\}\end{aligned} \tag{5.40}$$

where $G(y')$ and $J(y'')$ represent the decay of incident and reflected beams

respectively. These functions are expressed as

$$G[y'(y,z)] = 1 + \left(\frac{1}{\sqrt{2}} - 1\right) \frac{[y + sz - (y_1 + sz_1)]}{L\sqrt{s^2+1}} \quad (5.41)$$

$$J[y''(y,z)] = 1 + \left(\frac{1}{\sqrt{2}} - 1\right) \frac{[y - sz - (y_a + sz_a)]}{L\sqrt{s^2+1}} \quad (5.42)$$

where L is again the along-beam dissipation length. Assuming that dissipation occurs only in the superposition region for the central part of the beam, the dissipation length is proportional to the beam thickness parameter b. From the geometry,

$$L = \frac{2b}{s} = 10 \text{ km} \quad (5.43)$$

which is also representative of the beam horizontal width. As in Case I, L is required to be sufficiently greater than the horizontal beam width to satisfy the linearized perturbation equations (3.11) - (3.14) to first order. Hence, the validity of subsequent derivations may be subject to error.

The value of the decay functions ranges from 1 (no dissipation) to $\frac{1}{\sqrt{2}}$ (dissipated such that momentum-fluxes are halved) as shown in Figure 5.9 for $L = 10$ km. This formulation also satisfies the surface boundary condition, $\widetilde{w_2}(z=0) = 0$, since, along the surface $z = 0$ (i) $\eta = \beta$ and (ii) $y_1 = y_a$ which implies $G(y,0) = J(y,0)$. Finally, the time-mean meridional and vertical momentum-fluxes are

$$\langle \widetilde{v}^2_{sup} \rangle_t = \frac{\kappa^2 \left[G^2(b^2+\beta^2) + J^2(b^2+\eta^2) + 2GJ(b^2+\eta\beta)\right]}{2(s^2+1)(b^2+\eta^2)(b^2+\beta^2)} \quad (5.44)$$

$$\langle \widetilde{v}_{sup}\widetilde{w}_{sup} \rangle_t = \frac{s\kappa^2[G^2(b^2+\beta^2) - J^2(b^2+\eta^2)]}{2(s^2+1)(b^2+\eta^2)(b^2+\beta^2)} \quad (5.45)$$

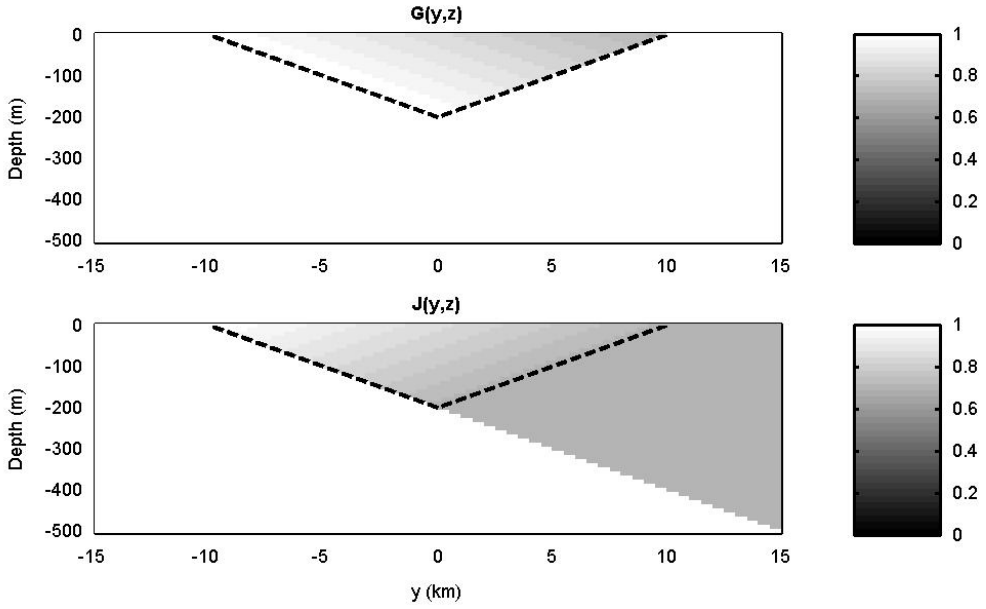

Figure 5.9: The decay functions for the incident beam $G(y, z)$ (upper panel) and reflected beam $J(y, z)$ (lower panel) in and around the dissipation region (dotted lines denote its edges) for dissipation length $L = 10$ km.

which reduce to Case II when $G = J = 1$. Partial derivatives are

$$\frac{\partial G}{\partial y} = \left(\frac{1}{\sqrt{2}} - 1\right) \frac{1}{L\sqrt{s^2+1}} \tag{5.46}$$

$$\frac{\partial G}{\partial z} = s\frac{\partial G}{\partial y} \tag{5.47}$$

$$\frac{\partial J}{\partial y} = \frac{\partial G}{\partial y} \tag{5.48}$$

$$\frac{\partial J}{\partial z} = -s\frac{\partial G}{\partial y}. \tag{5.49}$$

The forcing is

$$\begin{aligned}\frac{\partial \langle \widetilde{v}_{sup}^2 \rangle_t}{\partial y} + \frac{\partial \langle \widetilde{v}_{sup}\widetilde{w}_{sup} \rangle_t}{\partial z} = & \frac{\kappa^2}{(s^2+1)(b^2+\eta^2)(b^2+\beta^2)} \times \\ & \Big\{(s^2+1)[G(b^2+\beta^2) + J(b^2+\eta^2)]\frac{\partial G}{\partial y} + \\ & (G+J)(b^2+\eta\beta)\frac{\partial G}{\partial y} + GJ(\beta+\eta)\frac{\partial \eta}{\partial y} - \\ & GJ(b^2+\eta\beta)\frac{\partial \eta}{\partial y}\left(\frac{\eta}{b^2+\eta^2} + \frac{\beta}{b^2+\beta^2}\right)\Big\}\end{aligned} \tag{5.50}$$

which reduces to Case II for $G = J = 1$.

Assuming parameters values in Table 5.1 and force balance (3.39), forcing and zonal time-mean velocity are shown (Figure 5.10). Dissipation significantly influences the pattern of forcing. Forcing varies from -16.4×10^{-7} to 4.8×10^{-7} m/s^2. Time-mean zonal velocity ranges from -0.005 to 0.02 m/s, with eastward transport dominating. Inside the dissipating superposition region, flows are shifted eastward even though the range is nearly identical to Case II. The most significant changes from the non-dissipating case are along the inner 200 m of the beam, where the along-beam velocities are greatest. Outside, flows are the same as Case II except for a slight reduction after exiting the superposition region due to having momentum-fluxes

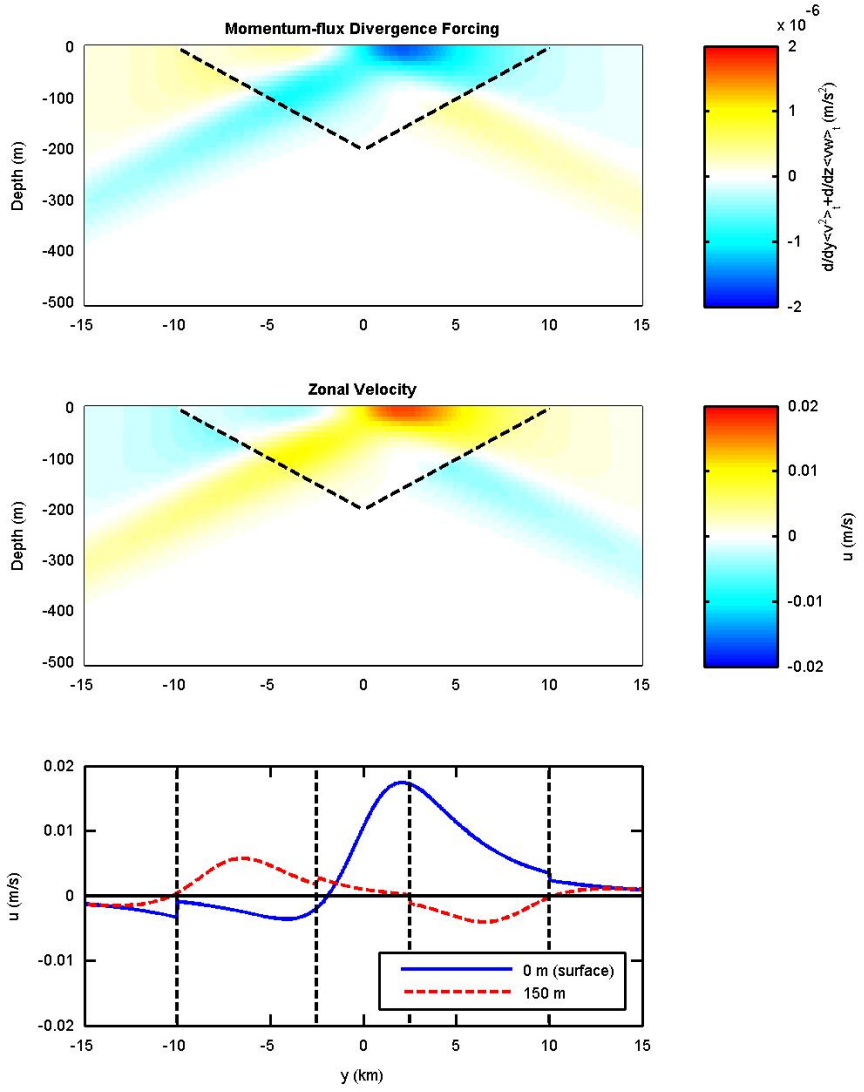

Figure 5.10: Momentum-flux divergence forcing (upper panel) and resulting time-mean zonal velocity (middle panel) caused by superposition of an upward-propagating beam and its reflection with dissipation through part of the superposition region. Horizontal profiles of time-mean zonal velocity (lower panel) at the surface (0 m) and 150 m depth show opposing jets and an eastward shift in velocities within the dissipation region. Dotted lines denote edges of the dissipating region, emphasizing abrupt discontinuities resulting from $G \neq 0$, $J \neq 0$.

halved. Horizontal profiles at the surface and 150-m depth illustrate the predominantly eastward flow and discontinuities at the edge of the dissipating region. Opposing jets are still present at the surface, although the eastward jet dominates.

By examining the separate contribution of each forcing function (5.50) term in the curly brackets (denoted $T1$ to $T4$; Figure 5.11), in comparison to their counterpart (5.34) in the non-dissipative case ($T3$ and $T4$; Figure 5.12), the eastward shift can be better understood. The first two terms, $T1$ and $T2$, are predominantly eastward and do not have a counterpart in the non-dissipative case due to the factor $\frac{\partial G}{\partial y}$. The last two terms, $T3$ and $T4$, are greater in magnitude and remain largely unchanged from the dissipative case, although magnitudes within and following the dissipative region are slightly diminished. Consequently, the eastward shift in the flow is driven by the first two terms, particularly by the rate of decay with distance.

5.4 Tracer Transport

Since time-mean tracer transport has been linked to dissipating internal waves (Andrews et al., 1987; Plumb and Mahlman, 1987), it is worth investigating whether there is tracer transport associated with Cases I, II and III. This analysis serves to compare our results to previous studies and to determine whether superposition introduces another transport mechanism.

Assume that the tracer, $\theta = \overline{\theta} + \widetilde{\theta}$, is conservative (i.e., $\frac{D\theta}{Dt} = 0$). Following the approach to 9.4.3 in Andrews et al. (1987), we average over one wave

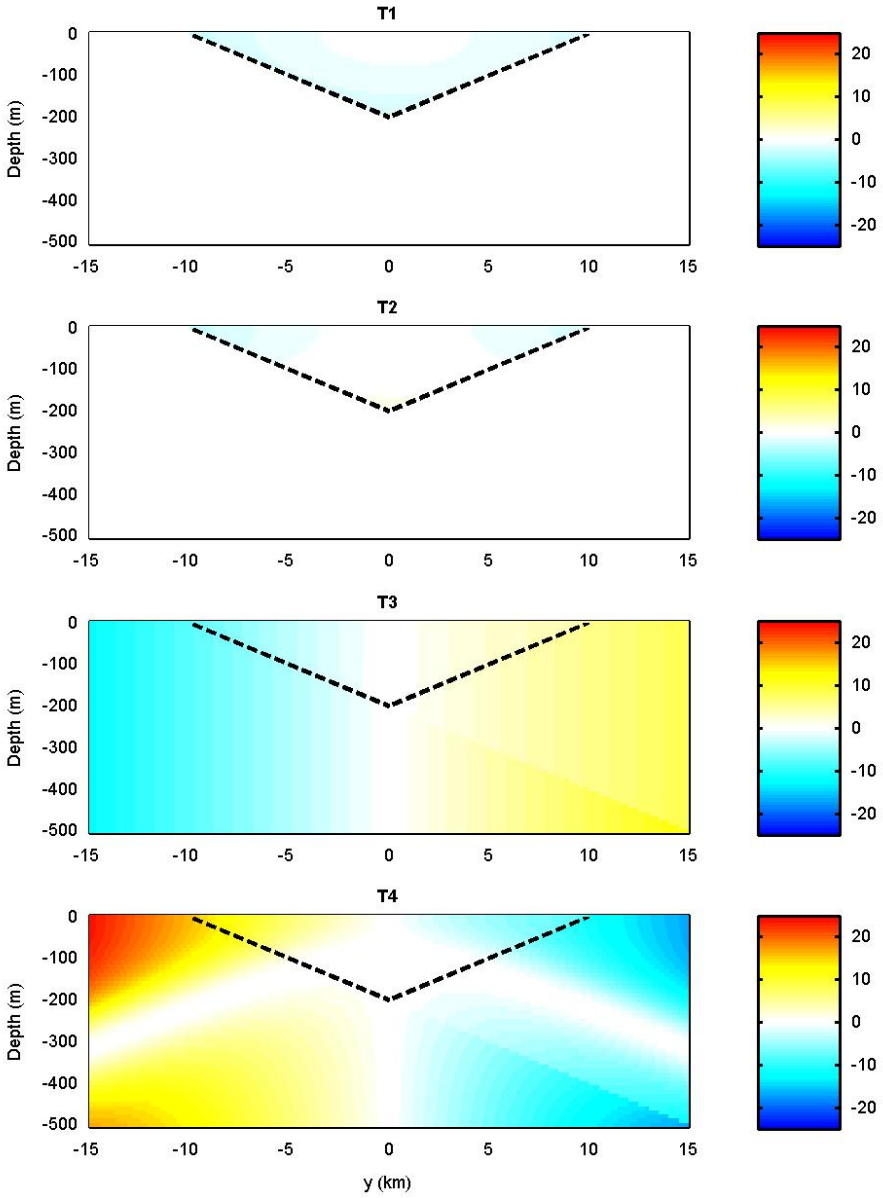

Figure 5.11: Relative contribution of each forcing function (5.50) term in the curly brackets (denoted $T1$ to $T4$). Dotted lines denote edges of the dissipating region.

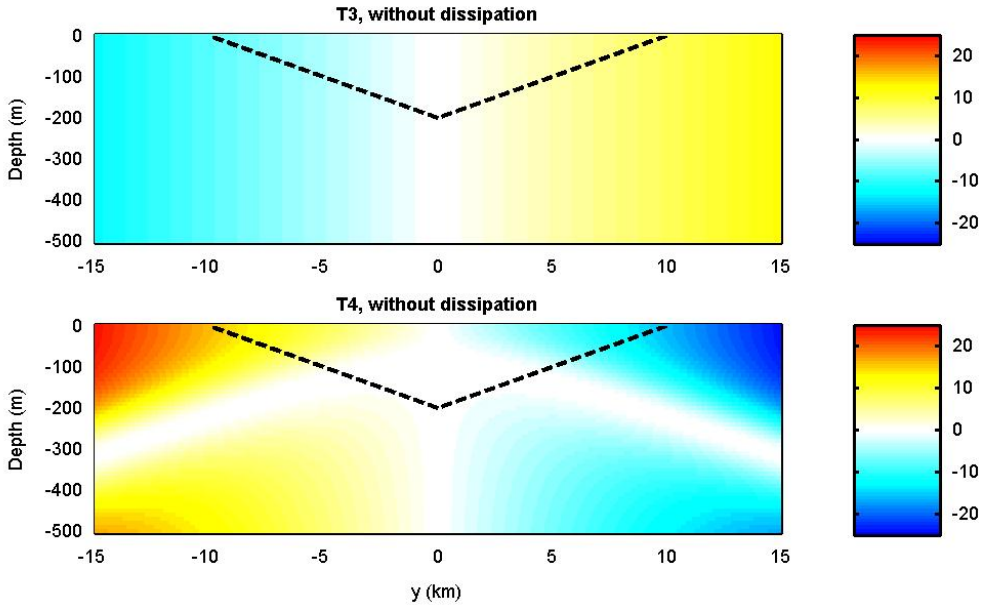

Figure 5.12: Relative contribution of non-dissipative forcing function (5.50) terms ($T3$ and $T4$), corresponding to (5.50). Dotted lines denote edges of the dissipating region.

period and let $\overline{v} = \overline{w} = 0$ to obtain

$$\frac{D\overline{\theta}}{Dt} = \frac{\partial\overline{\theta}}{\partial t} + \overline{u}\frac{\partial\overline{\theta}}{\partial x} = -\frac{\partial}{\partial x}\langle\widetilde{u}\widetilde{\theta}\rangle_t - \frac{\partial}{\partial y}\langle\widetilde{v}\widetilde{\theta}\rangle_t - \frac{\partial}{\partial z}\langle\widetilde{w}\widetilde{\theta}\rangle_t \tag{5.51}$$

where only the tracer concentration varies zonally. The material derivative $\frac{D}{Dt}$ is the sum of the Eulerian time-derivative $\frac{\partial}{\partial t}$ and the advection terms (e.g., $\overline{u}\frac{\partial}{\partial x}$). The Eulerian derivative is the rate of change at a fixed point, while the material derivative is the rate of change following a fluid parcel.

The oscillatory part of the tracer $\widetilde{\theta}$ can be expressed in terms of the wave velocities

$$\widetilde{\theta}_{\pm} = \left[\frac{-f}{\omega^2}\frac{\partial\overline{\theta}}{\partial x} + \frac{i}{\omega}\left(\frac{\partial\overline{\theta}}{\partial y} \pm s\frac{\partial\overline{\theta}}{\partial z}\right)\right]\widetilde{v}. \tag{5.52}$$

where plus refers to northward-upward propagation and minus northward-downward propagation.

We begin with Case I, the dissipative upward-propagating beam. Before and after the dissipating patch, the mean Lagrangian derivative $D\overline{\theta}/Dt = 0$. Consequently, the mean Eulerian time-derivative of the time-mean tracer quantity balances its mean zonal advection (i.e., $\frac{\partial\overline{\theta}}{\partial t} = -\overline{u}\frac{\partial\overline{\theta}}{\partial x}$) and both terms are zero since $\overline{u}$ is zero. The material and Eulerian mean time-derivatives are nonzero only for the dissipative section where the internal wave momentum-flux divergences drive a zonal mean flow. Substituting in the dissipating region internal wave velocities (5.16), we have

$$\frac{D\overline{\theta}}{Dt} = \frac{f}{\omega^2}\frac{\partial\overline{\theta}}{\partial x}\frac{\kappa^2}{L(b^2+\eta^2)}\left(\frac{1}{\sqrt{2}} - 1\right)\frac{1}{\sqrt{s^2+1}}G(y'). \tag{5.53}$$

Using $\overline{u}$ obtained for Case I, we find that

$$\frac{D\overline{\theta}}{Dt} = \frac{\partial\overline{\theta}}{\partial t} + \overline{u}\frac{\partial\overline{\theta}}{\partial x} = -\frac{f^2}{\omega^2}\frac{\partial\overline{\theta}}{\partial x}\overline{u} \tag{5.54}$$

which does not equal zero for $\frac{\partial\overline{\theta}}{\partial x} \neq 0$. This implies that the tracer concentration time-mean material derivative is the opposite sign as the zonal mean velocity if $\frac{\partial\overline{\theta}}{\partial x} > 0$. Conversely, the tracer concentration time-mean material derivative is the same sign as the zonal mean velocity if $\frac{\partial\overline{\theta}}{\partial x} < 0$. It follows that

$$\frac{\partial\overline{\theta}}{\partial t} = -\left(1 + \frac{f^2}{\omega^2}\right)\frac{\partial\overline{\theta}}{\partial x}\overline{u} \tag{5.55}$$

where the first and second terms are due to advection and dissipation respectively and are additive. At a given location, the time-mean tracer concentration is also changing in time and $|\ \frac{\partial\overline{\theta}}{\partial t}\ | > |\ \frac{D\overline{\theta}}{Dt}\ |$. In fact, the ratio between $\frac{\partial\overline{\theta}}{\partial t}$ and $\frac{D\overline{\theta}}{Dt}$ is $\frac{\omega^2}{f^2} + 1$, which has a minimum of 2 when $\omega \sim f$ and becomes very large for $\omega \gg f$. It equals 3.24 for M_2 internal waves at Mendocino Escarpment. Again, an eastward (westward) flow implies a decreasing (increasing) concentration. This result agrees with the non-transport theorem for the atmosphere (Andrews et al., 1987) which states that dissipation is required for Eulerian time-mean changes in tracer concentrations.

For Case II (surface reflection without dissipation), there is an eddy transport within the superposition region. The oscillatory part of the tracer is

$$\begin{aligned}\widetilde{\theta}_{sup} &= \frac{-f}{\omega^2}\frac{\partial\overline{\theta}}{\partial x}\frac{\kappa}{\sqrt{s^2+1}(b^2+\eta^2)(b^2+\beta^2)}\left\{b\cos(\omega t)(2b^2+\beta^2+\eta^2)\right. \\ &\quad \left. + \sin(\omega t)[\eta(b^2+\beta^2) + \beta(b^2+\eta^2)]\right\}. \end{aligned} \tag{5.56}$$

It follows that

$$\frac{D\overline{\theta}}{Dt} = \frac{f}{\omega^2}\frac{\partial\overline{\theta}}{\partial x}\frac{s\kappa^2}{(s^2+1)^{1.5}(b^2+\eta^2)(b^2+\beta^2)}\Bigg[\beta+\eta- (2b^2+2\eta\beta)\left(\frac{\eta}{b^2+\eta^2}+\frac{\beta}{b^2+\beta^2}\right)\Bigg]. \quad (5.57)$$

Using $\overline{u}$ obtained for Case II, (5.54) and (5.55) hold as in the Case I dissipating region. Thus, both the material derivative and Eulerian time-derivative have the same relation to the zonal mean velocity as in Case I. If $\frac{\partial\overline{\theta}}{\partial x}$ is uniform initially and $\overline{u}$ is calculated using the triangular beam structure (Figure 5.8), the antisymmetry of the superposition region would create large tracer gradients in the y-direction near the ocean surface over time. This outcome of having tracer transport in the absence of dissipation does not violate the non-transport theorem (Andrews et al., 1987) because that theorem was for purely zonal flow and reflection superposition was not included. As mentioned previously in Case II, the Stokes drift may also serve to reduce the mean zonal flow and, hence, the tracer transport.

For Case III (surface reflection with dissipation), the oscillatory part of the tracer within the superposition region is

$$\widetilde{\theta}_{sup} = \frac{-f}{\omega^2}\frac{\partial\overline{\theta}}{\partial x}\frac{\kappa}{\sqrt{s^2+1}(b^2+\eta^2)(b^2+\beta^2)}\Big\{b\cos(\omega t)[G(b^2+\beta^2)+J(b^2+\eta^2)] + \sin(\omega t)[G\eta(b^2+\beta^2)+J\beta(b^2+\eta^2)]\Big\}. \quad (5.58)$$

It follows that

$$\begin{aligned}\frac{D\overline{\theta}}{Dt} &= \frac{f}{\omega^2}\frac{\partial\overline{\theta}}{\partial x}\frac{\kappa^2}{(s^2+1)(b^2+\eta^2)(b^2+\beta^2)}\times \\ &\left\{(s^2+1)[G(b^2+\beta^2)+J(b^2+\eta^2)]\frac{\partial G}{\partial y}+\right. \\ &(G+J)(b^2+\eta\beta)\frac{\partial G}{\partial y}+GJ(\beta+\eta)\frac{\partial \eta}{\partial y}- \\ &\left.GJ(b^2+\eta\beta)\frac{\partial \eta}{\partial y}\left(\frac{\eta}{b^2+\eta^2}+\frac{\beta}{b^2+\beta^2}\right)\right\} \qquad (5.59)\end{aligned}$$

From $\overline{u}$ obtained for Case III, we again have the relations (5.54) and (5.55). If $\frac{\partial\overline{\theta}}{\partial x}$ is uniform initially and $\overline{u}$ is similar to (Figure 5.10), flow in the superposition region would create large tracer gradients in the y-direction near the ocean surface over time. Moreover, a tracer with a positive zonal gradient would diminish most quickly in the fastest flowing jet (Figure 5.10).

From this assessment, there are three ways in which internal waves affect tracer transport: (i) tracer perturbations are induced by internal wave perturbations, and tracer concentrations change on subinertial time-scales due to both (ii) dissipation and (iii) superposition of internal wave beams for zonally inhomogeneous tracers. For (ii) and (iii), where there are internal wave-induced changes in mean circulation, the transport is proportional to mean-flow velocities and the ratio between mean Eulerian and Lagrangian derivatives is constant. This outcome implies that tracer transport is blind to the mechanism by which mean-flow is generated.

Chapter 6

Discussion

6.1 Results and Limitations

The above cases demonstrate that dissipation or superposition is required for momentum-flux divergence forcing to be nonzero. A narrower beam would enable greater forcing since the dissipation lengths could be reduced. For the upward-propagating and dissipating beam in Case I, induced flow is always eastward. Case II, a surface-reflected internal wave beam without dissipation, produced the most noteable results since this forcing and associated tracer transport were unexpected. Induced zonal velocities up to greater than 0.01 m/s occur in both directions. Even faster velocities would occur if the beam was narrower (as in Case I) or had greater peak amplitudes. However, the Stokes drift may negate this effect. The addition of dissipation (Case III) shifted the velocity field within the superposition region eastward. This eastward tendency reflects Case I results and causes peak zonal velocities of 0.02 m/s. Both dissipation and superposition can cause nonzero changes of mean tracer concentration over time following a parcel, assuming tracer

concentrations vary zonally. The ratio between Eulerian and Lagrangian mean tracer time-derivatives is constant. Tracer transport patterns within the dissipation and/or superposition regions are proportional to the velocity field. Thus, tracer transport does not directly depend on whether dissipation or superposition induce mean velocities, but simply requires their generation by internal waves.

Mendocino Escarpment observations motivated development of these case studies, but direct comparison requires caution and more data. We based the Ekman-like force balance (3.39) on the assumption that zonal variability, time-mean meridional velocities, and meridional pressure gradients are negligible. Zonal variability is difficult to discern from the data, but meridional and vertical energy- and momentum-fluxes dominate with magnitudes typically 2-3 times larger. Time-mean baroclinic meridional velocities are nonzero, including near the surface reflection at Station 8 where southward flow is evident. Meridional pressure gradients appear to be small based on the isopycnals in Figure 4.16, but horizontal resolution is sparse. Thus, there is uncertainty associated with this force balance despite some supporting evidence. Next, there are challenges in interpreting the data, due to potential aliasing with near-inertial frequency waves and insufficient data zonally. Most importantly, observations are too sparse meridionally, especially near the surface reflection, to adequately compare our results. If Station 8 is at the leading edge of the surface reflection superposition region, then we expect a weak time-mean westward flow and this is the case. However, other forcing mechanisms such as wind, density gradients and eddies cannot be ruled out. Because Mendocino Escarpment observations do not yet prove nor disprove the case studies, more data could provide useful clarification.

Specifically, dense measurements near and within the superposition region and additional information about the proportion of internal wave energy and momentum lost is required. A tracer experiment monitored carefully both spatially and temporally could validate the ratio between Eulerian and Lagrangian time derivatives of mean tracer concentrations and comparisons for the theoretical superposition cases.

Further theoretical work could examine a case without assuming a steady-state force balance (i.e., $\partial/\partial t \neq 0$), and allowing for a beam that is finite in the x direction (i.e., $\partial/\partial x \neq 0$). For a beam of sufficient zonal width, the force balance (3.39) would initially generate zonal flows as described in Cases II and III. However, horizontal gradients in time-mean zonal velocity and time-mean pressure would develop, generating time-mean meridional flows such that the continuity and u-momentum equations are satisfied. Stationary flows are likely to involve one or more vortices, although a detailed analysis is necessary to characterize flows. More physically realistic nonlinear dissipation and beam-shape parameterizations would also be beneficial.

6.2 Broader Impacts

There are numerous areas that could provide useful comparisons, particularly in regions known for intense internal tides. These locations include the Hawaiian Ridge, Virginia continental slope, Oregon continental slope, and Indonesian Seas.

The Hawaiian Ridge at Kauai Channel has steep topography and barotropic flow perpendicular to the ridge. Cole et al. (2009) established the existence of tidal beams generated at the ridge and persisting over a region which in-

cludes the first surface reflection. Their computations have similar features to Mendocino Escarpment: predominantly two-dimensional internal tides, enhanced inferred turbulent dissipation near the surface reflection and to a lesser degree along the beam path before the reflection, largest horizontal energy-fluxes near the surface reflection, and along-beam gradients in momentum-fluxes where beams interact with one another. In addition, they are able to show enhanced mean velocities within the beam path, particularly near the surface reflection. Based on the observations, they conclude momentum-flux divergences drive mean flows of 0.01 to 0.03 m/s, comparable to Case II and III results. They also reach the conclusion that beam interactions induce momentum-flux divergences capable of sustaining a mean flow in the absence of dissipation. However, there was no attempt to distinguish whether beam interactions, dissipation or their combination is responsible for their results. Their mean along-ridge horizontal velocity (Figure 6.1) is structurally similar (Figure 5.10) near the surface reflection; the mean flow on either side of the reflection is asymmetric with weaker negative flow in the negative direction near the incident beam, and much stronger flow in the positive direction near the reflected beam. This suggests that the combined influence of beam interactions and dissipation may be responsible, although wind-generated eddies (known to be strong in this region) are another possibility.

There are other regions where internal tides reflect off near-critical slopes, focusing the energy into a narrow band. Slightly supercritical slopes transmit the energy downward, while slightly subcritical slopes transmit the energy upward. This intensification promotes enhanced dissipation at surface or bottom reflections. For instance, Nash et al. (2004) observed enhanced dis-

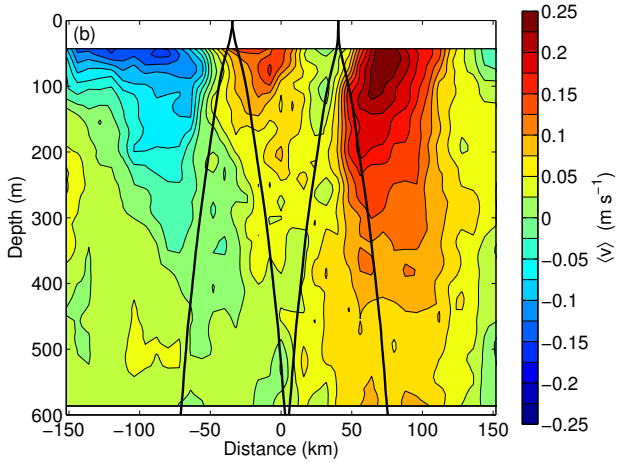

Figure 6.1: Mean along-ridge velocity at Kauai Channel, Hawaii (Cole et al., 2009). Permission for reprint received from S. Cole.

sipation near the base of the Virginia continental slope. They argue that a remotely-generated internal tide reflects from the near-critical part of the slope, dissipating as it is reflected off the bottom. The same effect may be responsible for mixing hotspots at near-critical slopes of the Oregon continental slope (Nash et al., 2007). This possibility is supported by far-field internal tide measurements, but the relative role of locally-generated tides is still unknown.

Simulations of the barotropic and baroclinic tides in the Indonesian Seas (Robertson and Ffield, 2007) indicate extensive interactions in tidal beam fields, including between the internal tide and its own reflections, to the extent that beams seldom propagate in isolation. They show a beam emanating from the Dewaking Sill which is postulated to be a region of intense tidal mixing. This beam displays peak velocities near the surface associated with strong vertical shears. If the dissipation is large in this region, it would be a good candidate for investigating whether internal tides are forcing mean flow as in Case III.

It may be worthwhile pursuing the significance of wave-mean forcing in tandem with mixing hotspots due to internal tides. Using single-beam soundings, Becker and Sandwell (2008) determined that 4.5% of the seafloor in the deep ocean (>2000 m) has a slope greater than the M_2 critical slope. This fraction is much higher than the 1.5% determined from satellite bathymetry. These regions are concentrated in the Southern Ocean, Indian Ocean and along the Mid-Atlantic Ridge.

Given our theoretical results and the abundance of similar situations throughout the oceans, localized forcing by internal tide momentum-flux diverengences merits further study.

Chapter 7

Conclusions

Previous studies demonstrating internal wave momentum-flux divergence forcing time-mean flows in the presence of dissipation (Eliassen and Palm, 1960; Holton and Alexander, 2000; Thorpe, 1999) in combination with Mendocino Escarpment observations (Althaus et al., 2003) motivate this study. Since earlier studies are limited with regard to wave-wave interactions (particularly at surface reflections) and a general theory does not exist, new derivations were necessary. Observations depict an internal tide beam emanating from the ridge, with elevated inferred dissipation rates (Althaus et al., 2003) near the first surface reflection, and diminished energy- and momentum-fluxes after it. Based on these observations, theoretical analysis involving simplifications to the equations of motion and case studies are used to predict mean flows. When an internal tide beam is propagating through a region with negligible horizontal time-mean velocities and pressure gradients parallel to its horizontal direction and neglible variability perpendicular to it, a force balance between the Coriolis force and internal tide momentum-flux divergences occurs (analogous to an Ekman balance). Case III predicts

mean zonal flows ∼0.02 m/s in the surface reflection superposition region for which there is no data. Typical wind-driven flow velocities are O(0.01-0.1) m/s, depending on latitude and wind speed. For the assumptions and parameters motivated from Mendocino Escarpment, the time-mean zonal velocity maintained by the force balance is comparable to wind-driven flow.

Beyond the implications for Mendocino Escarpment, there are three important points. First, internal wave-momentum flux divergences can induce non-negligible velocities. Second, superposition of internal wave beams can also generate non-negligible velocities in the absense of dissipation in contrast to previous results and expectations; these velocities may be balanced, at least in part, by the Stokes drift. Third, intense internal tide beams are common to many sites within the ocean, meaning interactions between internal tide beams may be an important mechanism for generating localized flows. This point is emphasized by the mean velocities evident at Kauai Channel (Cole et al., 2009) which support our findings. Similar analysis at other sites is vital to understanding the role of internal tide momentum-flux divergence forcing in the ocean.

Bibliography

[1] Althaus, A., E. Kunze and T. Sanford, 2003: Internal tide radiation from Mendocino Escarpment. *J. Phys. Oceanogr.*, **33**, 1510-1527.

[2] Andrews, D., J.R. Holton and C.B. Leovy, 1987: Middle Atmosphere Dynamics. Academic Press.

[3] Andrews, D.G., and M.E. McIntyre, 1976: Planetary waves in horizontal and vertical shear: The generalized Eliassen-Palm relation and the mean zonal acceleration. *J. Atmos. Sci.*, **33**, 2031-2048.

[4] Andrews, D.G., and M.E. McIntyre, 1978: An exact theory of nonlinear waves on a Lagrangian-mean flow. *J. Fluid Mech.*, **89**, 609-646.

[5] Baines, P.G., 1982: On internal tide generation models. *Deep-Sea Res.*, **29**, 307-338.

[6] Becker, J.J., and D.T. Sandwell, 2008: Global estimates of seafloor slope from single-beam ship soundings. *J. Geophys. Res.*, **113**, doi:10.1029/2006JC003879.

[7] Bell, T.H., 1975: Topographically generated internal waves in the open ocean. *J. Geophys. Res.*, **80**, 320-327.

[8] Biello, J.A., and A.J. Majda, 2005: A new multiscale model for the Madden-Julian oscillation. *J. Atmos. Sci.*, **62**, 1694-1721.

[9] Boccaletti, G., R. Ferrari and B. Fox-Kemper, 2007: Mixed layer instabilities and restratification. *J. Phys. Oceanogr.*, **37**, 2228-2250.

[10] Booker, J.R., and F.P. Bretherton, 1967: The critical layer for internal gravity waves in a shear flow. *J. Fluid Mech.*, **27**, 513-519.

[11] Boyd, J.P., 1976: The noninteraction of waves with the zonally averaged flow on a spherical Earth and the interrelationships of eddy fluxes of energy, heat and momentum. *J. Atmos. Sci.*, **33**, 2285-2291.

[12] Bretherton, F.P., 1969: On the mean motion induced by internal gravity waves. *J. Fluid Mech.*, **36**, 785-803.

[13] Bretherton, F.P., and C. Garrett, 1968: The propagation of wave trains in moving media. *Proc. Roy. Soc. A.*, **302**, 529.

[14] Buhler, O., and M.E. McIntyre, 2003: Remote recoil: a new wave-mean interaction effect. *J. Fluid Mech.*, **492**, 207-230.

[15] Carter, G.S., M.C. Gregg and M.A. Merrifield, 2006: Flow and mixing around a small seamount on Kaena Ridge, Hawaii. *J. Phys. Oceanogr.*, **36**, 1036-1052.

[16] Charney, J.G., and P.G. Drazin, 1961: Propagation of planetary-scale disturbances from the lower into the upper atmosphere. *J. Geophys. Res.*, **66**, 83-109.

[17] Cole, S.T., D.L. Rudnick, B.A. Hodges, and J.P. Martin, 2009: Observations of tidal internal wave beams at Kauai Channel, Hawaii. *J. Phys. Oceanogr.*, **39**, 421-436.

[18] Desaubies, Y., and M.C. Gregg, 1981: Reversible and irreversible finestructure. *J. Phys. Oceanogr.*, **11**, 541-556.

[19] De Silva, I.P.D, J. Imberger and G.N. Ivey, 1997: Localized mixing due to a breaking internal wave ray at a sloping bed. *J. Fluid Mech.*, **350**, 1-27.

[20] Eliassen, A., and E. Palm, 1960: On the transfer of energy in stationary mountain waves. *Geofys. Publikasjoner*, **22**, 1-23.

[21] Frankignoul, C., 1974: Observed anisotropy of spectral characteristics of internal waves induced by low-frequency currents. *J. Phys. Oceanogr.*, **4**, 625-634.

[22] Garrett, C., 1968: On the interaction between internal gravity waves and a shear flow. *J. Fluid Mech.*, **34**, 711-720.

[23] Garrett, C., and E. Kunze, 2007: Internal tide generation in the deep ocean. *Annu. Rev. Fluid Mech.* , **39**, 5787.

[24] Gerkema, T., 2001: Internal and interfacial tides: beam scattering and local generation of solitary waves. *J. Mar. Res.*, **59**, 227-255.

[25] Gerkema, T., F.A. Lam and L.R.M. Maas, 2004: Internal tides in the Bay of Biscay: conversion rates and seasonal affects. *Deep-Sea Res. II*, **51**, 2995-3008.

[26] Gill, A.E., 1982: *Atmosphere-Ocean Dynamics*. Academic Press, 662 pp.

[27] Hines, C.O., and C.A. Reddy, 1967: On the propagation of atmospheric gravity waves through regions of wind shear. *J. Geophys. Res.*, **72**, 1015-1034.

[28] Hogg, N.G., 1971: Longshore currents generated by obliguely incident internal waves. *Geophys. Fluid Dyn.*, **2**, 361-376.

[29] Holloway, P.E., and M.A. Merrifield, 1999: Internal tide generation by seamounts, ridges, and islands. *J. Geophys. Res.*, **104**, 25,937-25,951.

[30] Holton, J.R, 1974: Forcing of mean flows by stationary waves. *J. Atmos. Sci.*, **31**, 942-945.

[31] Holton, J.R, 1980: Wave propagation and transport in the middle atmosphere. *Philos. Trans. Roy. Soc. London, Series A, Mathematical and Physical Sciences*, The Middle Atmosphere as Observed from Balloons, Rockets and Satellites, **296**, 73-85.

[32] Holton, J.R., and M.J. Alexander, 2000: The role of waves in the transport circulation of the middle atmosphere. *AGU Monograph: Science Across the Stratopause*, 21-35.

[33] Hosegood, P., M.C. Gregg and M.H. Alford, 2006: Sub-mesoscale lateral density structure in the oceanic surface mixed layer. *Geophys. Res. Lett.*, **33**, doi:10.1029/2006GL026797.

[34] Jayne, S.R., and L.C. St. Laurent, 2001: Parameterizing tidal dissipation over rough topography. *Geophys. Res. Lett.*, **28**, 811-814.

[35] Javam, A., J. Imberger, and S.W. Armfield, 2000: Numerical study of internal wave-wave interactions in a stratified fluid. *J. Fluid Mech.*, **415**, 65-87.

[36] Jones, W., 1967: Propagation of internal gravity waves in fluids with shear flow and rotation. *J. Fluid Mech.*, **30(3)**, 439-448.

[37] Kunze, E., L.K. Rosenfeld, G.S. Carter and M.C. Gregg, 2002: Internal waves in Monterey Submarine Canyon. *J. Phys. Oceanogr.*, **32**, 1890-1913.

[38] Lamb, K.G., 2004: Nonlinear interaction among internal wave beams generated by tidal flow over supercritical topography. *Geophys. Res. Lett.*. **31**, doi:10.1029/2003GL019393.

[39] LeBlond, P.H., and L.A. Mysak, 1978: Waves in the Ocean. Elsevier Oceanography Series. Elsevier, 602 pp.

[40] Ledwell, J.R., E.T. Montgomery, K.L. Polzin, L.C. St. Laurent, R.W. Schmitt, and J.M. Toole, 2000: Evidence for enhanced mixing over rough topography in the abyssal ocean. *Nature*. **403**, 179-182, doi:10.1038/35003164.

[41] Lindzen, R., and J. Holton, 1968: A theory of the quasi-biennial oscillation. *J. Atmos. Sci.*, **25**, 1095-1107.

[42] Llewellyn-Smith, and S.G., W.R. Young, 2002: Conversion of the barotropic tide. *J. Phys. Oceanogr.*, **32**, 1554-1566.

[43] Lueck, R.G., and T.D. Mudge, 1997: Topographically induced mixing around a shallow seamount. *Science*, **276**, 1831-1833.

[44] McFarlane, N., 1987: The effect of orographically excited gravity wave drag on the general circulation of the lower stratosphere and troposphere. *J. Atmos. Sci.*, **44**, 17751800.

[45] McPhee-Shaw, E.E., and E. Kunze, 2002: Boundary-layer intrusions from a sloping bottom: A mechanism for generating intermediate nepheloid layers. *J. Geophys. Res.*, **107**, doi:10.1029/2001JC000801.

[46] Muench, J., and E. Kunze, 1999: Internal wave interactions with equatorial deep jets. Part I: Momentum flux divergences. *J. Phys. Oceanogr.*, **29**, 1453-1467.

[47] Muench, J., and E. Kunze, 2000: Internal wave interactions with equatorial deep jets. Part II: Acceleration of the jets. *J. Phys. Oceanogr.*, **30**, 2099-2110.

[48] Nash, J.D., E. Kunze, J.M. Toole and R.W. Schmitt, 2004: Internal tide reflection and turbulent mixing on the continental slope. *J. Phys. Oceanogr.*, **34**, 1117-1134.

[49] Nash, J., M. Alford and E. Kunze, 2005: Estimating internal wave energy fluxes in the ocean. *J. Atmos. Oceanic Technol.*, **22**, 1551-1570.

[50] Nash, J.D., M.H. Alford, E. Kunze, K. Martini and S. Kelly, 2007: Hotspots of deep ocean mixing on the Oregon continental slope. *Geophys. Res. Lett.*, **34**, doi:10.1029/2006GL028170.

[51] Petrelis, F., S. Llewellyn-Smith and W.R. Young, 2006: Tidal conversion at a submarine ridge. *J. Phys. Oceanogr.*, **36**, 1053-1071.

[52] Pingree, R.D., and A.L. New, 1991: Abyssal penetration and bottom reflection of internal tide energy in the Bay of Biscay. *J. Phys. Oceanogr.*, **21**, 28-39.

[53] Plumb, R.A., and J.D. Mahlman, 1987: The zonally averaged transport characteristics of the GFDL general circulation/transport model. *J. Atmos. Sci.*, **44**, 298327.

[54] Robertson, R., and A. Ffield, 2007: Baroclinic tides in the Indonesian seas: Tidal fields and comparisons to observations. *J. Geophys. Res.*, **113**, doi:10.1029/2007JC004677.

[55] Ruddick, B., and T.M. Joyce, 1979: Observations of interaction between the internal wavefield and low frequency flows in the North Atlantic. *J. Phys. Oceanogr.*, **9**, 498-517.

[56] Sanford, T., R. Driver, and J. Dunlap, 1985: An acoustic doppler and electromagnetic velocity profiler. *J. Atmos. Oceanic Tech.*, **2**, 110-124.

[57] Scinocca J.F., and N.A. McFarlane, 2000: The parameterization of drag induced by stratified flow over anisotropic orography. *Q. J. Roy. Meteor. Soc.*, **126**, 2353-2393.

[58] Scinocca, J.F., 2003: Low-level topographic drag in atmospheric flows. *Proceedings of the 13th 'Aha Huliko'a Hawaiian Winter Workshop*, Honolulu, HI, University of Hawaii at Manoa, 111-118.

[59] Sherman, J.T., and R. Pinkel, 1991: Estimates of the Vertical Wavenumber-Frequency Spectra of Vertical Shear and Strain. *J. Phys. Oceanogr.*, **21**, 292-303.

[60] Skyllingstad, E.D., and H.W. Wijesekera, 2003: Large-eddy simulation of flow over coastal ridges. *Proceedings of the 13th 'Aha Huliko'a Hawaiian Winter Workshop*, Honolulu, HI, University of Hawaii at Manoa, 107-109.

[61] Smith, W.H.F., and D.T. Sandwell, 1997: Global seafloor topography from satellite altimetry and ship depth soundings. *Science*, **277**, 1957-1962.

[62] Tandon, A, and C. Garrett, 1995: Geostrophic adjustment and restratification of a mixed layer with horizontal gradients above a stratified layer. *J. Phys. Oceanogr.*, **25**, 2229-2241.

[63] Teoh, S.G., G.N. Ivey and J. Imberger, 1997: Laboratory study of the interaction between two internal wave rays. *J. Fluid Mech.*, **336**, 91-122.

[64] Thorpe, S.A., 1997: On the interactions of internal waves reflecting from slopes. *J. Phys. Oceanogr.*, **27**, 2072-2078.

[65] Thorpe, S.A., 1999: The generation of alongslope currents by breaking internal waves. *J. Phys. Oceanogr.*, **29**, 29-38.

[66] U.S. Navy, cited 2009: Naval Oceanography Portal - Phases of the moon. [Available online at http://www.usno.navy.mil/USNO/astronomical-applications/data-services/phases-moon]

[67] Vlasenko, V., N. Stashchuik, and K. Hutter, 2005: Baroclinic Tides. Cambridge University Press, 351 pp.